RESEARCH: Review

Unveiling the structural origin to control resistance drift in phase-change memory materials

Wei Zhang [1,2,*], Evan Ma [3,*]

[1] Center for Advancing Materials Performance from the Nanoscale, State Key Laboratory for Mechanical Behavior of Materials, Xi'an Jiaotong University, Xi'an 710049, China
[2] Materials Studio for Neuro-inspired Computing, School of Materials Science and Engineering, Xi'an Jiaotong University, Xi'an 710049, China
[3] Department of Materials Science and Engineering, Johns Hopkins University, USA

The global demand for data storage and processing is increasing exponentially. To deal with this challenge, massive efforts have been devoted to the development of advanced memory and computing technologies. Chalcogenide phase-change materials (PCMs) are currently at the forefront of this endeavor. In this Review, we focus on the mechanisms of the spontaneous structural relaxation – aging – of amorphous PCMs, which causes the well-known resistance drift issue that significantly reduces the device accuracy needed for phase-change memory and computing applications. We review the recent breakthroughs in uncovering the structural origin, achieved through state-of-the-art experiments and *ab initio* atomistic simulations. Emphasis will be placed on the evolving atomic-level details during the relaxation of the complex amorphous structure. We also highlight emerging strategies to control aging, inspired by the in-depth structural understanding, from both materials science and device engineering standpoints, that offer effective solutions to reduce the resistance drift. In addition, we discuss an important new paradigm – machine learning – and the potential power it brings in interrogating amorphous PCMs as well as other disordered alloy systems. Finally, we present an outlook to comment on future research opportunities in amorphous PCMs, as well as on their reduced aging tendency in other advanced applications such as non-volatile photonics.

Materials for storage and processing in the big data era

In response to the increasing demand for data storage and processing driven by Artificial Intelligence (AI), 5G and other advanced data-intensive technologies, non-volatile memory and neuro-inspired computing devices are under active investigation and development. Novel materials to meet the challenges posed by these advanced devices are currently under intensive research, including phase-change chalcogenides [1–8], resistive-switching oxides [9–12], spintronic materials [13–15], ferroelectric materials [16–18], organic polymers [19–21], perovskites [22–24] as well as two-dimensional layered materials [25–31].

Among these competing candidates, chalcogenide phase-change materials (PCMs) based electronic random access memory (PRAM) are technologically more mature. The recently released PRAM products – 3D Xpoint – pioneered by Intel and Micron, have entered the global memory market, bridging the performance gap between flash memory and dynamic random access memory (DRAM). With further improvement on materials composition [32–34] or programming scheme [35–37], PRAM can compete with DRAM and cache memory in terms of programming speed, yet have orders of magnitude higher storage density and persistent storage capability when power off (non-volatile features) [1]. It has also been demonstrated recently that PRAM cell arrays can be used collectively for efficient emulation of artificial neurons and synapses [38–48], which could be used to accomplish arithmetic computing and complex AI tasks in

* Corresponding authors.
    E-mail addresses: Zhang, W. (wzhang0@mail.xjtu.edu.cn), Ma, E. (ema@jhu.edu).

memory units with substantial improvement on power, computing and areal efficiencies. Neuro-inspired or neuromorphic computing can be implemented at several different levels according to the degree of biological resemblance to the human brain [49]. For the basic level of co-location of memory and processing, it is also known as in-memory computing or computational memory [49–51]. PCMs are one of the leading candidates to satisfy the needs for such purposes.

Phase-change memory and computing

PRAM exploits the large contrast in electrical resistance between the amorphous and crystalline states of PCM to encode data [2]. A typical PCM array is shown in Fig. 1a. The amorphous state with higher resistance is designated as the logic state "0", while the crystalline state with lower resistance is then the logic state "1". The switching between the two solid states is very rapid and highly reversible, and is typically driven by Joule heating generated by an external voltage pulse. PCM undergoes an amorphous-to-crystalline transition during the SET or write operation, while the reverse uses the crystalline-to-amorphous transition via a liquid state, in the RESET or erase operation (Fig. 1b). Three major PCM materials families have been identified so far, and can be summarized in the Ge-Sb-Te ternary diagram shown in Fig. 1c [2]. The first family is located along the pseudo-binary line along GeTe and Sb_2Te_3. In addition to the commercialized,

flagship $Ge_2Sb_2Te_5$ (GST) alloy [52–54], GeTe, $Ge_1Sb_2Te_4$, $Ge_3Sb_2Te_6$, $Ge_8Sb_2Te_{11}$ and some off-stoichiometric Ge-Sb-Te alloys have also been heavily investigated [55–66]. Towards the Sb_2Te_3 end, dopant elements are typically needed to improve the thermal stability of the amorphous state [67–73]. Recently, Sc was incorporated into Sb_2Te_3 forming a $Sc_{0.2}Sb_2Te_3$ (SST), which on the one hand raised the crystallization temperature to the GST level, while on the other hand resulted in a sub-nanosecond SET speed through enhanced nucleation upon crystallization [32–34,74–77]. The other two families reside around Sb_2Te_1 and Sb, respectively, alloyed with elements such as Ag, In, Ge, Ga and others [78–86]. Representatives are $Ag_4In_3Sb_{67}Te_{26}$ (AIST) and $Ge_{15}Sb_{85}$, respectively.

Human brain consists of $\sim10^{11}$ neurons and $\sim10^{15}$ neuron interconnections—the synapses. This massively parallel computing architecture offers extraordinary computing efficiency, in particular for complex tasks such as image recognition and language translation. In recent years, progress in brain-like or neuro-inspired computing has been benefiting from the rapid development of AI technologies in terms of both advanced algorithms [87] and new hardware [88]. From the materials side, PCM offers simple implementations of neurons [42] and synapses [39] (Fig. 1d), which is of much higher areal and power efficiencies as compared with the current silicon-transistor-based devices, because each PCM cell can be switched in a continuous way with
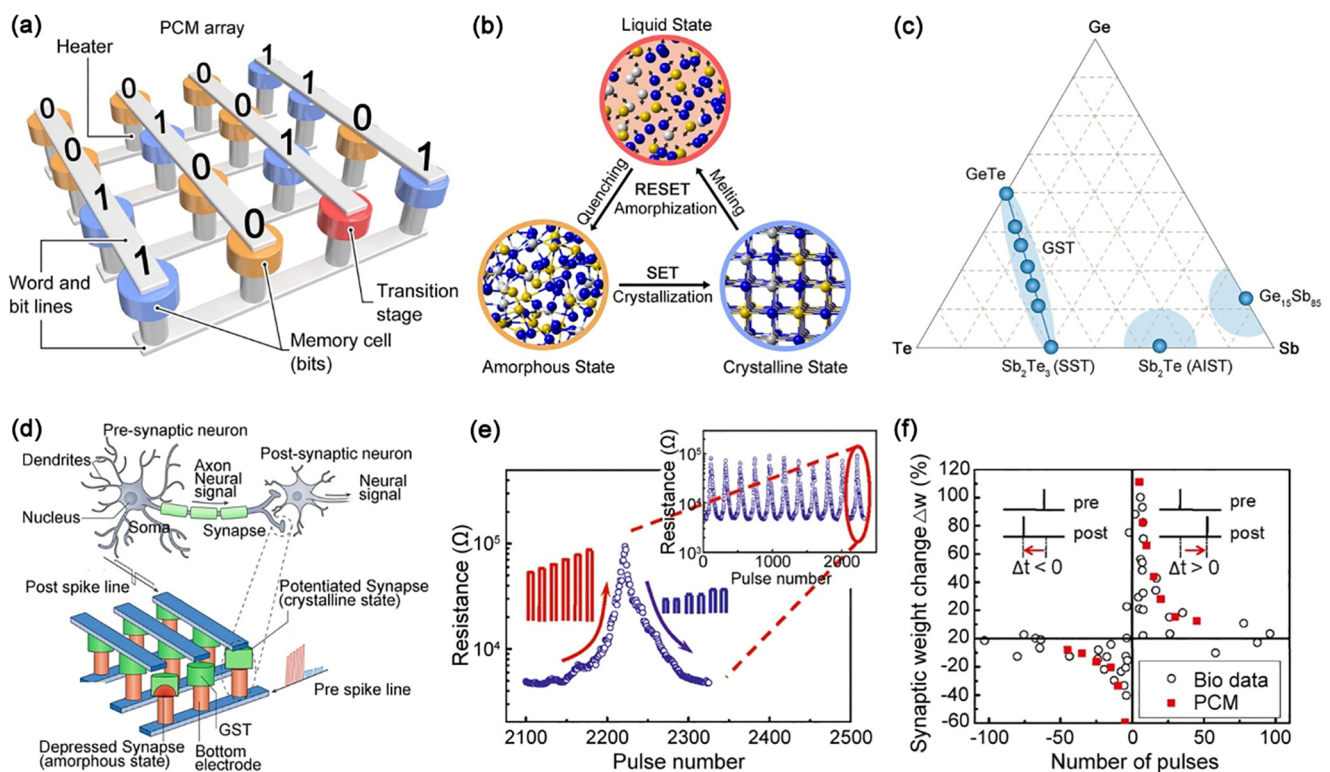
FIGURE 1

Concepts of phase-change memory and computing. (a) Sketch of a typical PCM array encoded in binary scheme. (b) The amorphous phase with high electrical resistance state is defined as "0", and the ordered crystalline phase with low electrical resistance as "1". SET operation is completed by crystallization, while RESET operation is achieved by melt-quench amorphization. (c) The Ge-Sb-Te ternary diagram. (d) Schematics of biological neurons (top) and the PCM array for the emulation of synapses (bottom). (e) Gradual RESET and gradual SET operation with a continuous change in resistance value. (f) Spike timing-dependent plasticity (STDP) learning rule emulated using PCM cells, yielding a close comparison with biological data. The synaptic weight is represented by the conduction of PCM cells. Panels (d)–(f) are adapted with permission from Ref. [39], ACS.

gradual changes in electrical resistance, going beyond the traditional binary scheme [49]. Instead of sending single pulses to SET or RESET each memory cell, a train of voltage pulses with varied amplitude and width can be applied to tailor the phase fractions in each PCM cell through partial SET or RESET. Given the large electrical resistance (conductance) contrast (by a factor of 10^3–10^6) between the amorphous state and the crystalline state, the gradual phase transition delivers a sizable change in resistance along with increasing pulses (Fig. 1e). This continuous (i.e., multi-step) phase change can be used to efficiently emulate the behaviors of neurons and synapses, such as integrate-and-fire functionality [42] and spike-timing dependent plasticity (STDP) [39]. Fig. 1f shows the emulation of STDP using a single PCM cell per synapse, where the electrical conductance of PCM cell is used to represent the synaptic weight [39]. The overall electrical data closely resemble the biological counterpart.

Aging and resistance drift

Amorphous PCMs can be obtained by magnetron sputtering or by very rapid quenching from the melt with a high cooling rate ∼10^9 K/s. They are typically bad glass formers with very strong tendency towards crystallization [89–92]. This makes it difficult to determine their glass transition temperature T_g: the T_g for amorphous GST has been estimated to be in the range of 100–200 °C [93–97]. Nevertheless, all amorphous PCMs exhibit a clear spontaneous structural relaxation during prolonged service (aging), causing the well-known resistance drift issue [98–116], which hampers further optimization of PRAM for ultrahigh stor-

age density and phase-change neuro-inspired computing (PCNIC) devices of high programming consistencies [117–119]. This obviously motivates an in-depth understanding of the amorphous structures involved, in particular the structural changes before and after aging, to unveil the origin of relaxation and devise solutions to bring the drift under control. Much progress in this regard has been achieved in recent years, which will be summarized in this article. Our review will follow a "from science to solutions" approach. More specifically, our viewpoints will be articulated via a concise presentation of the understanding gained to date, with regards to the amorphous structure of PCMs and its evolution upon aging. With this underpinning of fundamental knowledge, we then outline new strategies that have been shown to reduce, or feasible designs that are promising to control, the structural relaxation and resistance drift. For other related advances on fundamentals of PCMs, including crystallization kinetics and dynamical fragility [120–125], metavalent bonding and property contrast [126–129], disorder-induced phenomena and metal–insulator transition [130–135], interfacial memory and topological physics [136–140] of PCMs, the readers are referred to other comprehensive treatments, including the thorough reviews on corresponding issues in Refs. [1,141–148].

We reiterate that the reason to single out this aging and drift issue lies with its major impact on device performance. This is illustrated using Fig. 2 as an example. By increasing the amplitude of RESET pulse (Fig. 2a), the volume ratio of amorphous and crystalline phase can be altered gradually. Then multiple
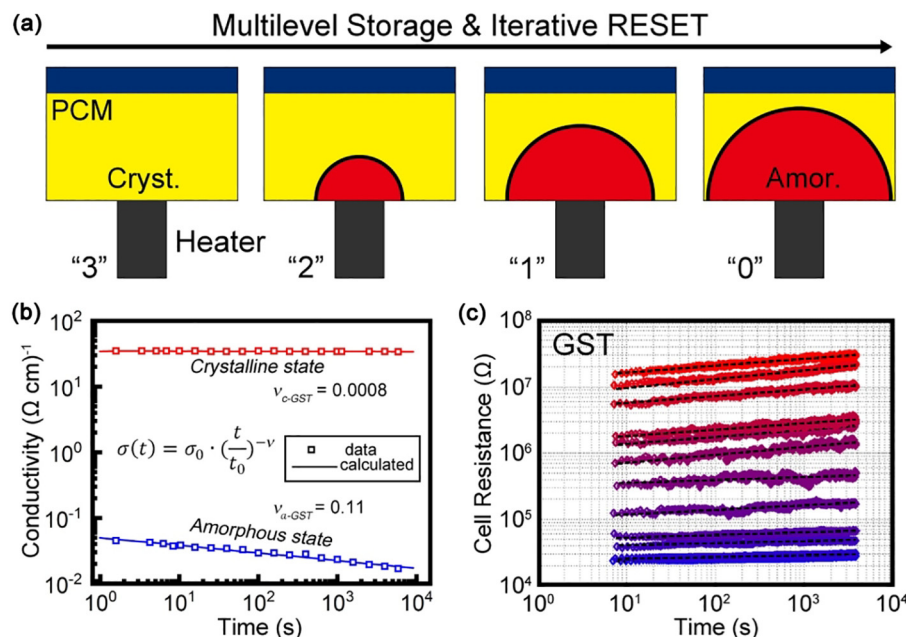
FIGURE 2

Gradual amorphization in the cell and resistance drift in the already-amorphized region. (a) Gradual amorphization of a PCM cell using voltage pulses at a varied amplitude. The ratio of amorphous to crystalline fractions results in multiple resistance levels, allowing and defining multiple states. Such a scheme is known as multilevel storage for PRAM, or iterative RESET for neuro-inspired computing. (b) The resistance drift issue (plotted in conductivity) of amorphous GST. Over time the resistivity (conductivity) of the crystalline state is stable, while the resistivity (conductivity) of the amorphous state increases (decreases). While this results in an enlarged contrast window in binary storage, it becomes a major problem when multiple states are in use: the drift leads to decoding errors, as shown in (c) where some of the resistance profiles of 11 states in a GST cell overlap with neighboring ones after tens of seconds. Panels (b) and (c) are adapted with permission from Ref. [104] and Ref. [49], AIP.

states with distinctly different resistance level can be defined in a single mushroom-type PCM cell. Such multilevel storage scheme could drastically increase the volume of data when using the same set of memory arrays, going beyond the binary storage scheme [7]. For the crystalline state, the measured cell resistivity or conductivity is stable over long service cycles, but in the amorphous state, the resistivity (conductivity) increases (decreases) continuously and steadily over time. The resistance (conductance) of the amorphous state follows a temporal dependence $R(t) = R_0 (t/t_0)\nu$ ($\sigma(t) = \sigma_0 (t/t_0)^- \nu$), where R_0 (σ_0) is the resistance (conductance) measured at any time t_0 greater than a few hundreds of ns after the RESET operation. The drift coefficient ν is ~0.11 for amorphous GST measured at room temperature (Fig. 2b) [104]. Note that aging in amorphous PCM is not a slow crystallization process. Upon aging, the amorphous phase in fact moves towards lower energy state but deviates further away from the crystalline counterpart, as the resistance contrast gets enlarged, rather than reduced. The drift issue does not affect binary storage, but hinders the multilevel implementation. If we divide the whole contrast window into more than 10 levels, these resistance states are distinguishable over the initial tens of seconds, but afterwards, the steady increase in the resistance of the N state could enter the resistance window of the $N + 1$ state [49], causing decoding errors (Fig. 2c).

For neuro-inspired computing, this partial amorphization process is termed as iterative RESET operation (Fig. 2a). A PCM array can be directly used to make arithmetic operation such as matrix–vector multiplication [149]. To resolve an equation $Ax = b$, the elements of matrix A can be mapped by the conductance values of PCM cells in a crossbar configuration (Fig. 1a), the values of vector x can be encoded into the amplitudes or durations of voltage pulses, and then the result b can be obtained by measuring the resulting electrical currents according to the Ohm's law and Kirchhoff's current law [149]. However, the accuracy and efficiency of such computing task are largely affected by the drift issue, which changes the resistance (or conductance) value of every memory cell in an uncontrollable and undesirable manner during collective programming. Therefore, an in-depth understanding of the origin of aging in amorphous PCMs is of pressing need.

Modeling and measurements

Owing to the highly disordered nature and the complex chemical composition, the investigation of amorphous PCMs is particularly challenging. In this regard, density functional theory (DFT) based *ab initio* molecular dynamics (AIMD or DFMD) simulations have played an important role [150], as they allow the calculation of interatomic forces with quantum mechanics accuracy at every MD step. This approach has been widely applied to investigate the structural and properties of amorphous PCMs [151–186]. Typical AIMD simulations using standard plane-wave based DFT codes can support model size up to a few hundreds of atoms, over a few hundreds of picoseconds simulation time. With special optimization in computing scheme using advanced DFT codes for PCMs, AIMD simulations can study models of several hundreds of atoms over a few nanoseconds

simulation time [187–191]. Structural factors and various optical and vibrational spectra can be calculated using AIMD models and then be used to compare with X-ray diffraction and absorption, Raman spectroscopy, photothermal deflection spectroscopy, transmission electron microscopy and other experiments. In addition, reverse Monte Carlo analysis constrained to experimental data is also occasionally used to build amorphous models or refine AIMD results.

Structural features and aging mechanisms in amorphous PCMs

Modeling of amorphous GeTe

We start our discussion with a prototypical PCM – GeTe. Before talking about the evolution with aging, let us begin with a detailed description of the bonding and atomic structure in this amorphous alloy. Fig. 3a shows a 216-atom model of amorphous GeTe (18.9 Å in box edge length), generated by a melt-quench AIMD simulation [192]. This amorphous phase was obtained starting from the perfect crystalline phase, which was heated to 2000 K to fully remove the crystalline order, then equilibrated at the melting T ~900–1000 K, and finally quenched to room temperature with a rapid cooling rate of ~10^{11} K/s. Structural data such as radial distribution function (RDF) or g(r), angular distribution function (ADF), and coordination number (CN) are collected, and the amorphous models are further relaxed at zero K prior to the electronic structure calculations, such as density of states (DOS) and chemical bonding crystal orbital overlap population (COOP) or crystal orbital Hamilton population (COHP) analyses [193–196], as shown in Fig. 3.

Amorphous GeTe is shown to be a narrow-gap semiconductor with multiple mid-gap states, as confirmed by the modulated photocurrent (MPC) experiments [197–199] and the DFT-calculated DOS [192] shown in Fig. 3b. The nature of covalent interactions is revealed via COOP analysis, with which the bonding (stabilizing) contributions to the electronic band structure are identified by positive orbital overlaps, while the antibonding (destabilizing) ones by negative orbital overlaps. As shown in Fig. 3b, the overall COOP indicates that most of bands below Fermi level are occupied by bonding states. The antibonding peak right below the Fermi level also appears in the corresponding rhombohedral crystalline phase [200], and as such would not play a major role in the atomic structure of amorphous GeTe. COOP can be calculated for each individual pair of atoms, and the integration of the specific COOP along the energy axis up to the Fermi level, $B_{AB} = \int_{-\infty}^{E_F} COOP_{AB}(E)dE$, termed as bond population B_{AB}, can distinguish the positive and negative covalent interactions between each pair of atoms. The distribution of the bond population shows a clear decay as the interatomic distance gets larger (Fig. 3c). A bond-weighted distribution function (BWDF) can be obtained by multiplying the g(r) with the bond population, $BWDF = \sum_{B>A}[\delta(r - |\mathbf{r}_{AB}|) \times B_{AB}]$, which presents a clear cutoff for chemical bonds in amorphous GeTe [200], i.e. 3.06 Å for Ge-Ge bonds, 3.16 Å for Ge-Te bonds, and no bonding interaction is found for Te-Te contacts (Fig. 3d). The BWDF method, as well as the use of electron localization function
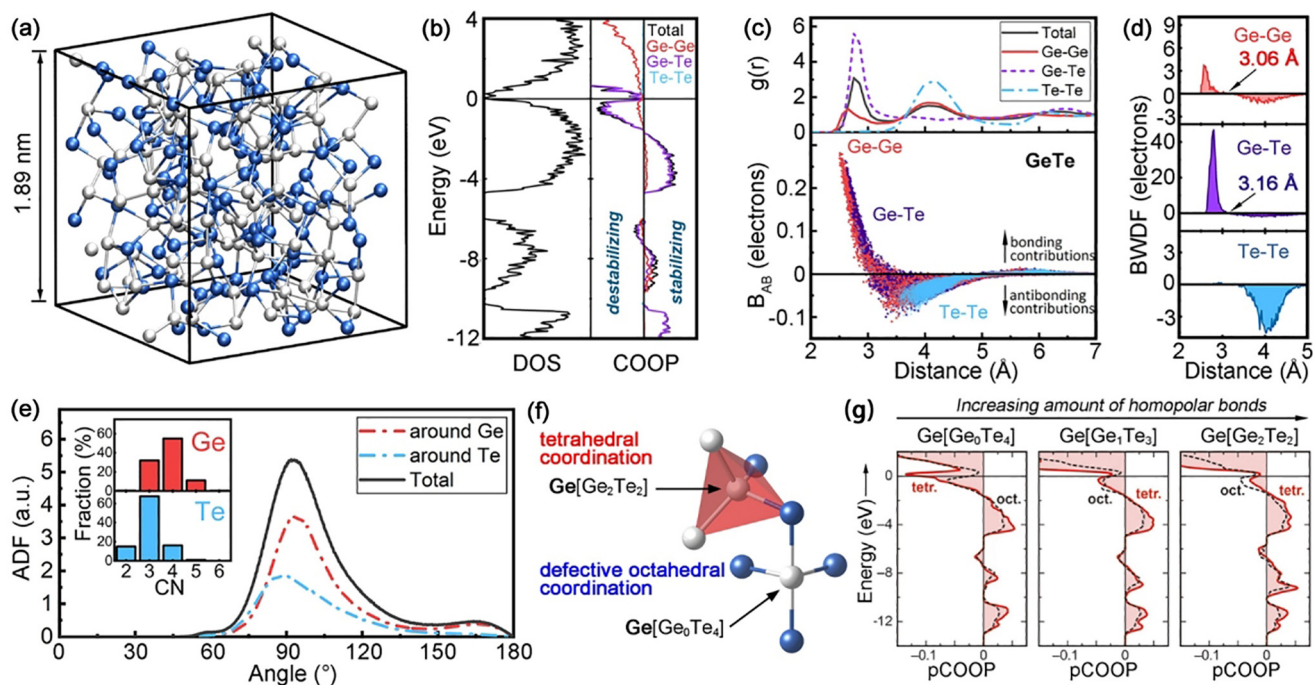
FIGURE 3

Ab initio modeling of amorphous GeTe. (a) An amorphous GeTe of 216 atoms generated by melt-quench AIMD simulations. Ge and Te atoms are rendered with gray and blue spheres. (b) Density of states (DOS) and crystal orbital overlap population (COOP), (c) radial distribution function g(r) and bond population B_{AB}, (d) bond-weighted distribution function (BWDF) and (e) angular distribution function (ADF) and distribution of coordination number (CN) of amorphous GeTe. (f) A tetrahedral Ge motif and a four-fold defective octahedral Ge motif. (g) COOP projected over tetrahedral Ge motifs and four-fold defective octahedral Ge motifs with and without Ge-Ge homopolar bonds. Panels (b)–(e) are adapted with permission from Ref. [192], RSC. Panels (f) and (g) are adapted with permission from Ref. [200], Wiley-VCH.

(ELF) [153] or charge density difference [201] analysis, can reduce the arbitrariness when choosing bond cutoff for structural analyses.

Fig. 3e shows ADF and CN distribution of amorphous GeTe. The Ge- and Te-centered local motifs are primarily four- and three-fold coordinated. The ADF of Te shows a peak value at 90°, while that of Ge shows a shift towards larger value. A detailed analysis over each individual local motif reveals that Te atoms are mostly octahedrally coordinated as that in the crystalline phase, but with deficient number of neighbors. Ge atoms are found in both (defective-) octahedral (~70%) and tetrahedral (~30%) bonding configurations [152] (Fig. 3f). The presence of tetrahedral Ge in amorphous GeTe and GST had been under debate for more than a decade [151-153,202–208], as no crystalline germanium tellurides can be found in tetrahedral coordination [209]. It was discovered in AIMD simulations that the vast majority of tetrahedral Ge motifs were associated with at least one Ge-Ge homopolar bond [151,152], and the role of Ge-Ge homopolar bonds was later quantitatively assessed using COOP method [200]. As shown in Fig. 3g, Ge-Ge homopolar bonds drastically reduce the antibonding interaction at the Fermi level. It is now a consensus in the field that these homopolar bonds are formed in the molten state, due to the small heat of mixing of GeTe, and are frozen in and give rise to a fraction of tetrahedral Ge units upon rapid quenching. This understanding also implies that the tetrahedral units are ultimately transient in nature and may evolve with time.

Resistance drift in amorphous GeTe
The atomic structure picture above sets the stage for explaining the significant temporal drift in electrical resistance consistently observed in amorphous GeTe at ambient temperatures. Upon thermal annealing above room temperature but well below the crystallization temperature (T_x ~185 °C), the aging process is accelerated [210]. In the experiment shown in Fig. 4a, the amorphous sample was annealed at different temperatures below 130 °C for 1 h before the resistivity measurements at 120 K [211]. A continuous increase in resistivity relative to the initial value (dashed line) is observed upon the aging treatment. Photothermal deflection spectroscopy (PDS) measurements show a clear widening of optical band gap upon aging [211], as shown in Fig. 4b, which is in line with the ellipsometry measurements [212]. Using the melt-quenched model by AIMD simulation discussed above, the absorption spectrum can be computed using time-dependent DFT, which however shows strong absorptions at low energies (green curve in Fig. 4c) [211]. This deviation is due to the different thermal history of experimental sample and theoretical model. However, it is simply not feasible to carry out direct AIMD simulations on the time scale of seconds to hours.

Simulations to unravel aging mechanisms
A chemical substitution scheme was developed to model the aging path in amorphous GeTe in Ref. [211]. Since homopolar bonds are considered as "wrong" bonds in GeTe, the strategy
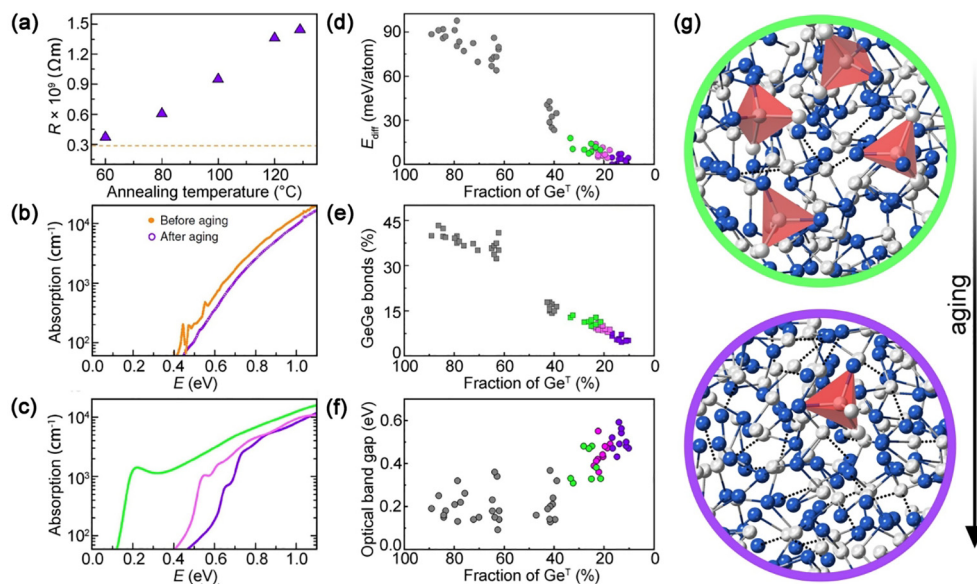
FIGURE 4

Aging mechanisms in amorphous GeTe. (a) The measured resistivity of amorphous GeTe thin film aged at different annealing temperatures. The transport measurement was done at 120 K. (b) Experimental absorption spectra from photothermal deflection spectroscopy (PDS) measurements in amorphous GeTe thin film before and after aging. (c) Simulated absorption spectra on AIMD generated melt-quench amorphous GeTe model (green), substituted GeSe (pink) and substituted SnTe (purple) amorphous GeTe models. The total energy (d), fraction of Ge-Ge bonds (e) and optical band gap (f) as a function of the fraction of tetrahedral Ge motifs in melt-quench amorphous (green), substituted GeSe (pink), substituted SnTe (purple) and substituted SiTe (gray) in amorphous GeTe models. Note here that the substitution with Si promotes homopolar bonds, tetrahedral units, higher energy but smaller optical band gap. (g) Atomic picture of aging in amorphous GeTe, showing a reduction of tetrahedral Ge motifs (highlighted by red polyhedron) and the reinforcement of Peierls distortion (long bonds are indicated by dashed lines). Panels (a)–(f) are adapted with permission from Ref. [211], Springer Nature Limited.

was to remove them to relax amorphous models to lower energy. To this end, the simulation took advantage of homologue compounds SnTe and GeSe, which have a higher heat of mixing and thus a larger energy penalty on homopolar bonds formation. Using the same lattice parameter as amorphous GeTe, melt-quench simulations were carried out to obtain amorphous SnTe and GeSe. Then Sn and Se atoms were substituted with Ge and Te atoms in these two sets of models. The new amorphous GeTe models were then equilibrated at room temperature and quenched down to zero K.

The GeTe model formed as such to mock aging relaxation, Fig. 3d–f, shows an effective reduction in total energy, fraction of homopolar bonds and tetrahedral units Ge^T and an increase in optical band gap (pink subst.GeSe, purple subst.SnTe) with respect to the standard melt-quenched model (green) [211]. The mid-gap states in melt-quenched models caused by tetrahedral Ge units are also no longer found in the substituted models. Ten configurations were considered for each set of simulations, and all the trends were the same. In addition to the removal of homopolar bonds and the disappearance of tetrahedral Ge units, the reinforcement of Peierls distortion also accompanies the aging of GeTe. Peierls distortion is typically found in crystalline PCMs and other semiconductors. Such distortion lowers the crystal symmetry by forming long and short bonding pairs over a ~180° bond angle, which typically leads to a widening of the band gap.

The simulated absorption spectra using the GeSe and SnTe substituted amorphous GeTe models yielded a much closer comparison with the experimental data [211] (Fig. 4c). Moreover, a

reduction in internal mechanical stress was observed in the aged GeTe samples [210], which was also reproduced in the substituted models. Amorphous GeTe models before and after aging are depicted in Fig. 4g, in which tetrahedral Ge units and Peierls distortions are highlighted. The removal of Ge-Ge homopolar bonds and four-fold Ge coordination was concluded to be the origin of the resistance drift (increase) in amorphous GeTe, based on *ab initio* simulations in combination with other simulation techniques including metadynamics [213] and Metropolis algorithms [214]. The mid-gap state by Ge-Ge chains was also confirmed by artificial bond rearrangement in an amorphous GeTe model generated by atomic distortion in the crystalline state [215]. Upon aging, the reduction of mid-gap states and the widening of band edge together lead to a decrease in conductivity, as the activation energy for electrical transport is increased [216]. A recent X-ray absorption work on amorphous GeTe however points towards an increase in Ge-Ge homopolar bonds upon aging [217]. This discrepancy with previous works could be attributed to the appearance of amorphous Ge sub-nuclei in the aged GeTe thin films due to the slight Ge-excess incorporated by magnetron sputtering [217].

The presence of homopolar Ge-Ge bonds is also reported to result in dynamical heterogeneities in the supercooled liquid state of GeTe, where the spatially dispersed local regions with long Ge-Ge chains move faster than other regions at 500 K, indicating a secondary (β) relaxation [218]. β-relaxation refers to the fast motions of a group of atoms inside a slow-mobility matrix, where the primary (α) relaxation processes take place at a much longer time scale [219–222]. Very recently, powder mechanical

spectroscopy experiments confirmed the presence of β-relaxation in amorphous GeTe, GST and AIST [223]. Upon heating above 350 K, an excess wing appears in the loss modulus spectrum as a function of temperature at a given frequency of sinusoidal stress, indicating the existence of β-relaxation taking place in local less ordered or less constrained regions where the collective motion of atoms can be more easily executed [223]. One is tempted to directly correlate this β-relaxation with the disappearing tetrahedral Ge illustrated in our aging discussion above. However, the two do not necessarily have a one-to-one correspondence, as amorphous AIST also shows a clear excess wing feature but has no homopolar Ge-Ge bonds. In other words, the exact mechanisms underlying β -relaxation in amorphous PCMs can possibly be multiple and should be systematically explored. The excess wing was found to vanish when the composition of GeTe was tuned towards non-PCM chalcogenide glasses such as GeSe and $Ge_{15}Te_{85}$ [223]. This result suggests that the better networked covalent bonds in the latter cases, more rigid than those in the inhomogeneous amorphous structure of PCMs, tend to suppress β-relaxation.

Bonding and local motifs in amorphous GST

Next, we discuss in detail the amorphous structure and its evolution in the commercialized workhorse PCM, $Ge_2Sb_2Te_5$ (GST). Along the same line as GeTe, we start with the bonding and local structural motifs in amorphous GST. Fig. 5a shows the comparison between the experimental [203] and theoretical [151] X-ray scattering factor $S(Q)$, where the theoretical calculation was made using a AIMD melt-quenched GST model. The good agreement of structural factor confirms that the overall structural feature of amorphous GST is well captured by AIMD simulation. Similar to amorphous GeTe, the major structural motifs in amorphous GST are also the three- and four-fold defective octahedral motifs around Te and Ge/Sb atoms (inset in Fig. 5a). A careful measure of local packing using bond order parameters also reveal that around 1/3 Ge atoms are tetrahedrally coordinated in amorphous GST (Fig. 5b). Similar to amorphous GeTe, very few tetrahedral Ge atoms are found to bond with Te atoms only. All the Ge atoms with more than one wrong bond, either Ge-Ge or Ge-Sb, are found in the tetrahedral geometry [151,152]. A detailed comparison of projected DOS in amorphous GST also shows that the average over Ge atoms presents a shape rather similar to the p-bonded Sb atoms (Fig. 5c), rather than the Ge atoms in diamond cubic Ge crystal, where sp^3 bonding is the dominant feature [153]. By integrating the site- and orbital-projected DOS within the core region, it was shown that all three-fold Ge units and a fraction of four-fold Ge units are (defective-) octahedrally bonded with the rest of four-fold Ge units being tetrahedrally coordinated (Fig. 5d).

Regarding the medium-range order in amorphous GST, the primitive rings analysis (inset in Fig. 5b) indicates that four-fold rings are the dominant structural fragments, which are regarded as precursors for rapid nucleation [152]. The recrystallized phase is in a cubic rocksalt structure with a high content of atomic vacancies, 10% in $Ge_2Sb_2Te_5$ [53,224]. In the amorphous phase, ~12% of the total volume is vacant, as shown by the cyan spheres in Fig. 5c. Fig. 5d indicates the distribution of these cavities (voids), with smaller ones dominating in the sam-

ple (red: liquid state at 900 K, black: amorphous state at 300 K). Its inset presents the void-void correlation function [152]. The excessive vacant volume in amorphous GST could promote the diffusion of atoms for rapid crystal growth in GST at elevated temperatures. Besides, the resistivity of amorphous GST can be drastically reduced by about four orders of magnitude by squeezing out these voids under hydrostatic-like pressure over 8 GPa, with no crystallization involved [225].

Mid-gap states in amorphous GST

Similar to amorphous GeTe, mid-gap defect states are found both in experiments and simulations for GST. However, in this alloy the structural origin of these mid-gap states still remains inconclusive. From an earlier AIMD work, mid-gap states were occasionally captured in some rapid-quenched amorphous GST models, where the electron wave function mostly appeared along some Sb-Te chains [226]. In a more recent theoretical work [227], the statistical sampling as well as the model size were significantly improved with the help of a machine-learning based interatomic potential developed specifically for GST [228]. All the amorphous models were relaxed further at zero K and their electronic structure calculations were performed using DFT. Mid-gap states were consistently found in all the amorphous models. The DOS and IPR—inversed participation ratio, a direct measure of localization of the wave function for each electronic state, of the 900-atom amorphous GST model [227] is shown in Fig. 6a. However, in this set of simulations, 5-coordinated Ge atoms are found to account for the local defective bonding configuration. Fig. 6b shows a typical local structural pattern for charge localization, which represents a crystalline-like atomic environment in the amorphous network. This picture is very different from the situation in amorphous GeTe, where the mid-gap states are found to be induced by tetrahedral defects that are absent in the crystalline counterparts. It is noted that the fraction of tetrahedral Ge motifs is typically lower in these new amorphous models (~11%) than that of standard AIMD simulations (~33%), therefore, it remains to the further explored whether these localized states around 5-coordinated Ge atoms can be reproduced by full AIMD simulations. In addition, direct aging simulations, similar to those done for amorphous GeTe, are anticipated to further clarify the relaxation mechanisms in amorphous GST.

Aging in amorphous GST

The presence of mid-gap states introduces charge traps, and their disappearance together with the widening of optical band gap are claimed to be the origin of resistance drift in amorphous GST [108,197]. It has been reported that X-ray absorption near-edge structure (XANES) can distinguish tetrahedral and defective octahedral Ge sites in the amorphous phase [229–231], in particular, from the L_3-edge spectra [231]. To assess the structural changes upon aging, several thin-film GST samples were annealed at temperatures ranging from 40 to 110 °C for 24 h. XANES measurements were then carried out immediately at room temperature after the aging treatment. As shown in Fig. 7a, a progressive and monoatomic change in the Ge L_3-edge XANES spectra is observed in the samples treated with higher annealing temperatures, indicating a gradual transforma-
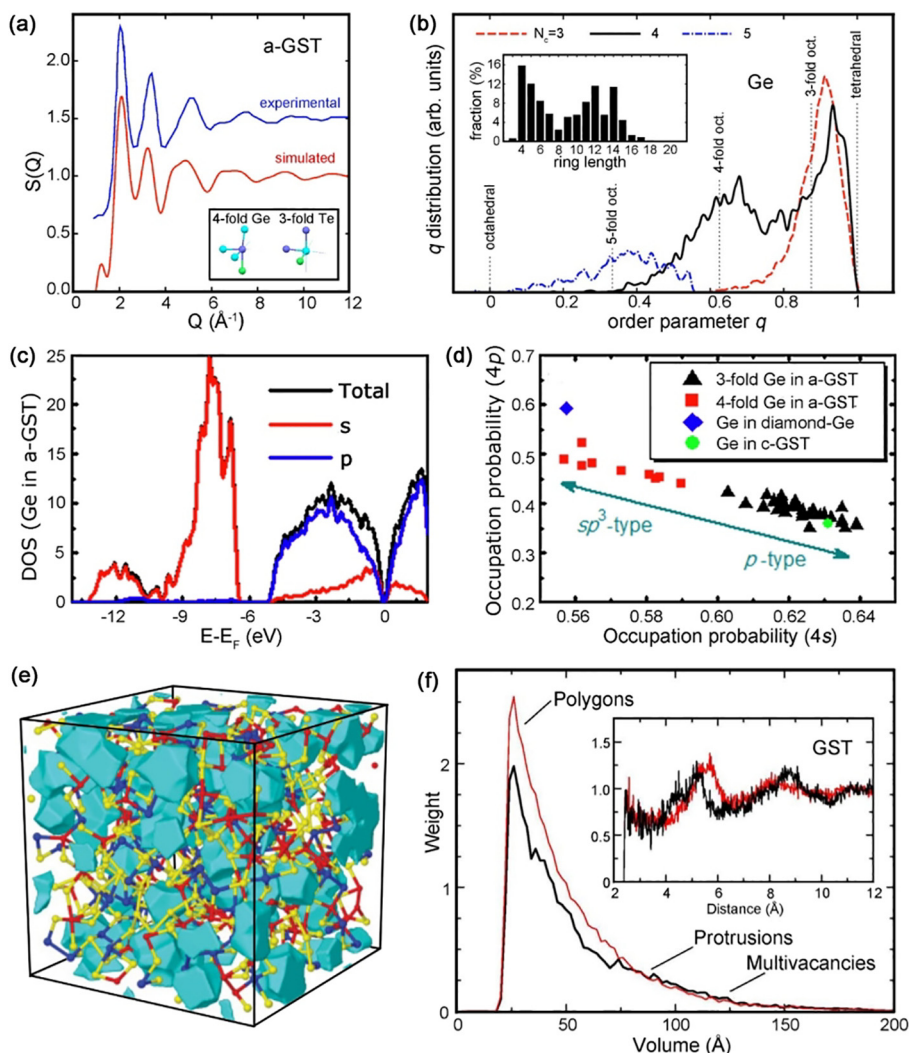
FIGURE 5

Ab initio modeling of amorphous GST. (a) The measured and simulated structural factor $S(Q)$ of amorphous GST. Four-fold and three-fold defective octahedral Ge and Te motifs are shown in the inset. (b) Distribution of the bond order parameter q, which has different characteristic values for different local motifs such as the tetrahedral and defective octahedral Ge environments. Inset, the primitive rings analysis of amorphous GST. (c) Partial DOS of Ge element in amorphous GST. (d) The occupation probability of 4s and 4p electrons for different structural motifs in crystalline Ge, amorphous and crystalline GST. (e) The amorphous GST structure, with voids highlighted in cyan. (f) The distribution of voids as a function of their volume size, and the void-void correlation function (inset), in liquid (red) and amorphous GST (black). Panels (a) and (b) are adapted with permission from Ref. [151], AIP. Panels (c)–(f) are adapted with permission from Ref. [153], Ref. [161] and Ref. [152], APS.

tion of tetrahedral sites towards defective octahedral sites (Fig. 7b) with reduction in Ge-Ge homopolar bonds. The XANES spectrum of the more aged sample yields a closer comparison with that of the recrystallized rocksalt phase, but with larger deviation in electrical resistance [231].

High-resolution transmission electron microscope (TEM) experiments have provided useful information in understanding the structural features in PCMs. In Ref. [232], the local structure of amorphous GST thin films was studied by carrying out nano-beam electron diffraction and radial distribution function analysis. The nearest neighbor peak at 2.8 Å and bond angle at 93.4° indicated that most of atoms are in a defective octahedral configuration. In Ref. [233], the combined high-resolution TEM experiments using an angstrom-beam electron diffraction (ABED) technique, local reverse Monte Carlo (local RMC) modeling

and AIMD simulations further confirmed this observation. As displayed in Fig. 7c–h, despite the typical halo rings features of disordered structures, clear four-, two- and six-fold symmetry that resemble the octahedrally bonded rocksalt phase features were captured in typical ABED patterns of amorphous GST. The intensity profile accumulated only from these three types of patterns was shown to be quite similar to the intensity profile of the overall amorphous structures. Together with theoretical modeling, it was concluded that the majority local arrangements in amorphous GST are in defective octahedral configurations, but with quite large degree of atomic distortion. It was not thoroughly assessed whether the minor fraction of tetrahedral Ge units existed or not, and it remained unclear whether the sample was aged or not, prior to the TEM experiments [233]. Nevertheless, these measurements are consistent with the theoretical
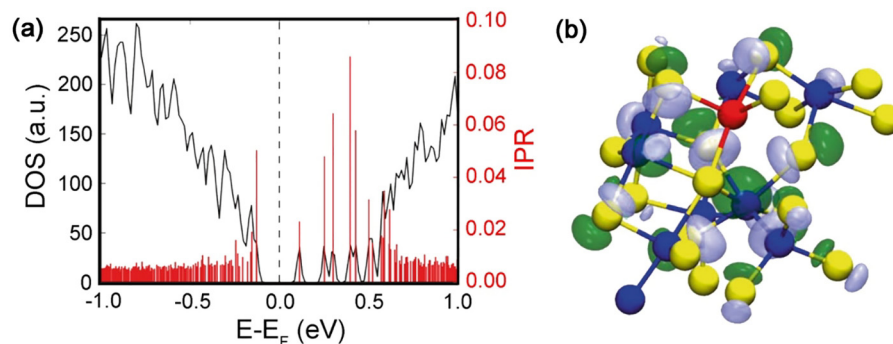
FIGURE 6

Mid-gap defect states in amorphous GST. (a) DOS and IPR of a 900-atom amorphous GST model. The amorphous model was generated by a machine-learning interatomic potential, which was further relaxed and calculated using DFT at zero K. (b) The local structure and molecular orbital associated with the mid-gap electronic state identified in the band gap of 900-atom amorphous GST model. Five- and six-coordinated Ge atoms are involved in the localization of the mid-gap state. Ge, Sb and Te atoms are rendered with blue, red and yellow spheres, respectively. The light blue and green isosurfaces represent the localized wave functions. Adapted with permission from Ref. [227], Springer Nature Limited.
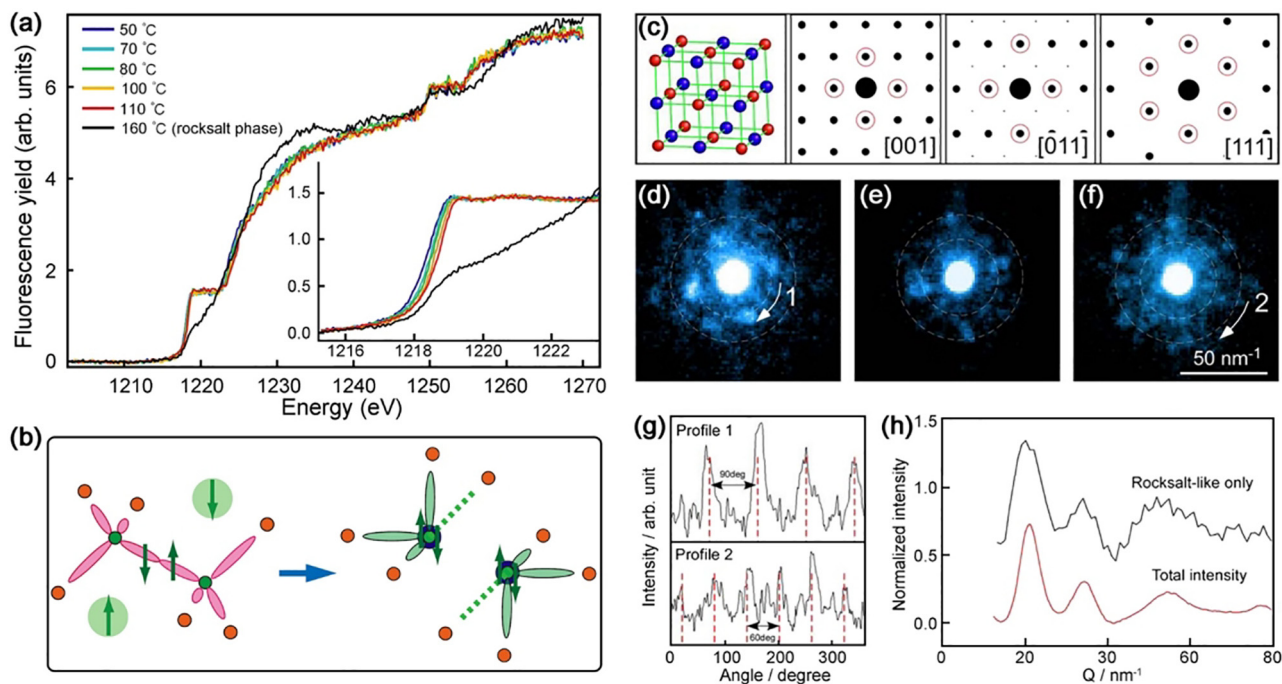

FIGURE 7

Structural measurements for amorphous GST. The X-ray absorption near-edge structure (XANES) measured for the Ge L_3-edge in amorphous GST upon aging treatment at different temperatures. (b) Sketch of the structural relaxation path from tetrahedral Ge sites towards defective octahedral Ge sites, as interpreted from the XANES data. (c) Sketch of a rocksalt GST with calculated diffraction patterns of the [0 0 1], [0 1 1], and [111] crystallographic orientation. (d)–(f) Three typical angstrom-beam electron diffraction (ABED) patterns measured in amorphous GST thin films, showing distorted octahedral features. (g) Intensity profiles of ABED patterns along circumferential directions indicated by arrows 1 and 2 in (d) and (f). (h) Total intensity (red) and accumulated intensity only with distorted octahedral ABED patterns. Panels (a) and (b) are adapted with permission from Ref. [231], AIP. Panels (c)–(h) are adapted with permission from Ref. [233], APS.

modeling results in that the defective octahedral units are the dominant structural motifs in amorphous GST, but with larger distortion with respect to its crystalline counterpart.

To recapitulate what has been summarized in this section, disappearing homopolar bonds (and tetrahedral Ge units) and reinforced Peierls distortion have been identified as two major relaxation mechanisms for both amorphous GeTe and GST upon aging. At present the jury is still out as to the possible role of other structural motifs, including Sb-Te chains and five-fold

crystalline-like Ge coordination that could induce mid-gap states in amorphous GST, in aging and resistance drift. Moreover, the structural origin of aging in PCMs that are not Ge-containing, such as Sb_2Te_3, SST and the other two families residing around Sb_2Te_1 and Sb, awaits future exploration. Nevertheless, the valuable insight acquired thus far at the atomic level has already been able to provide much-needed guidance, in conceiving new tactics to circumvent the drift problem, as will be discussed in the next section.

Strategies to alleviate the resistance drift

Here in this section, we discuss four recently attempted strategies from both device engineering and materials optimization stand-points. The success that has already been achieved through these informed device/materials design innovations reinforces the mechanistic concepts discussed above, and at the same time underscores the tremendous value of understanding the structural origin in pushing the limit of low resistance drift of the amorphous PCMs.

Strategy I – Device engineering

A few device engineering and programming schemes, including pre-programming [35], multi-PCM cell implementation [234] and mix-precision computing [149], have been developed to improve the crystallization speed, and to reduce or bypass the device-to-device variation issue of PCM devices. Regarding the resistance drift issue, a projected memory scheme has been developed [235–237], which does not suppress the intrinsic structural relaxation of amorphous PCM, but bypass the resistance drift issue for programming. The first report was in Ref. [235], which covered the GST memory cells with a metal nitride surfactant layer, to provide an alternative low-resistance current path when the cell is in the amorphous state. This approach was further developed and the concept of projection was clearly proposed and demonstrated in Ref. [236]. The essential idea is to decouple the information-encoding process from the information-retrieval process so that the resistance drift over time does not affect multilevel recording and reading.

As shown in Fig. 8a, electrical current passes through PCM vertically in a standard line cell setup, no matter whether the cell is in SET or RESET state. When the line cell is covered by a projection material with an intermediate resistance level between the crystalline and amorphous state of PCM, as shown in Fig. 8b–d, electrical current would pass through the parallel low-resistance projection segment during reading, if the internal PCM segment is in the amorphous phase. To read the resistance of the SET state and to perform the RESET operation, electrical current would pass through the crystalline PCM segment solely because of its low resistance. Importantly, to SET the memory cell, the electrical current would still pass through the PCM segment, because the resistance of amorphous PCM changes in a non-linear fashion as the voltage amplitude increases, known as Ovonic threshold switching effects [238], and becomes more conductive than the projection material before crystallization takes place (Fig. 8c). Therefore, the major role of the projection material is to re-route the reading of the RESET state of the memory cell. The larger the amorphous volume, the higher fraction of the projection segment that the electrical current passes through, thus overall larger cell resistance. Since no drift in resistance is present in the projection material, the accuracy of multilevel storage or iterative RESET of the projected PCM cell is significantly improved [236].

Growth-type PCMs, such as AIST and GeTe, were used to demonstrate the concept of projected memory cell. As shown in Fig. 8e, the drift coefficient v of amorphous AIST in the line cell is ~0.061 at measured at constant ambient temperature, but gets drastically reduced to ~0.003 in the projected memory
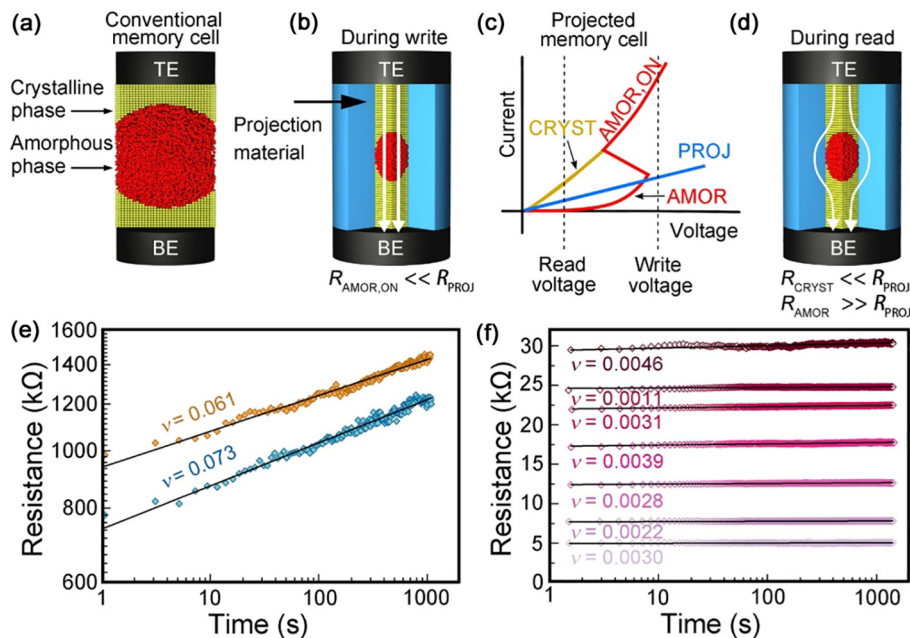
FIGURE 8

Projected PCM device. (a) A standard line cell PCM device. (b)–(d) The concept of projected PCM device. The line cell is covered by a non-insulating projection material, which has an intermediate resistance level in-between the crystalline phase and the amorphous phase of the PCM. Exploiting the threshold switching property of amorphous PCM, the electrical current flows through the projection surrounding at low voltages, but passes through the amorphous PCM part at high voltages. (e) Programmed states in AIST-based line cell with significant resistance drift at constant ambient temperature. (f) Programmed states in AIST-based projected memory cell with strongly reduced resistance drift coefficient v, by more than one order of magnitude with respect to (e), at constant ambient temperature. Adapted with permission from Ref. [236], Springer Nature Limited.

cell. Multiple programmed states show distinct resistance levels in the AIST-based projected memory cell over 1400 s [236], as shown in Fig. 8f. Based on this concept, an eight-bit precision in-memory scalar multiplication operation was successfully demonstrated using 12 conductance states of a GeTe-based projected memory device [239]. Moreover, a neural-network-based pattern classification task involving 30 such devices was accomplished with high accuracy [239]. Further attempts to improve the number of programming level and to use other PCMs, such as nucleation-type GST and SST alloys, are anticipated in future projected PCM devices.

Strategy II – Compositional tuning

Although the device manufacturing discussed above could help bypass the drift issue, it increases the complexity when it comes to mass production. In addition, it remains unclear whether such projection scheme can work stably over millions to billions of cycles that required for practical applications. A materials-based strategy is therefore desirable. This requires tailoring of the aging property of amorphous PCM directly, while keeping the overall device setup that is mature for mass production unchanged. Compositional tuning in the PCM is typically the route to alter the amorphous structure, so as to achieve the reduction in the drift coefficient of the amorphous state.

Take GeTe as an example. The drift coefficient ν of amorphous GeTe thin films was measured to be 0.129 at 50 °C. Upon alloying with Sn, the drift coefficient ν was reduced effectively to 0.095 and 0.053 for amorphous $Ge_3Sn_1Te_4$ and $Ge_1Sn_1Te_2$ thin films at 50 °C [240], respectively, as shown in Fig. 9a. Such a suppression of resistance drift can be understood as due to the reduction of the driving forces for aging. Melt-quenched AIMD simulations reveal that the fraction of tetrahedral Ge units gets gradually decreased with increasing Sn substitution of Ge, from ~30% in amorphous GeTe to ~7% in amorphous SnTe, and the vast majority of local motifs in amorphous SnTe are defective octahedral Sn units, as shown in Fig. 9b. This trend in structural change stems from the larger charge transfer between Sn and Te atoms with respect to that between Ge and Te atoms [192]. The higher electrostatic interactions in turn increase the energy penalty of homopolar bonds formation, leading to lower fraction of tetrahedral units in amorphous SnTe. As a consequence, the probability to obtain mid-gap states in amorphous $Ge_1Sn_1Te_2$ and SnTe models is largely reduced. This observation is consistent with the MPC measurements, where the defect state density is found to decrease in amorphous $Ge_xSn_{1-x}Te$ thin films as the fraction of Sn content increases [240].

Besides tetrahedral defects, the other driving force for aging in amorphous GeTe – Peierls distortion – is also weakened upon Sn alloying. In the amorphous phase, the degree of Peierls distortion can be assessed by calculating the angular-limited three-body correlation (ALTBC, normalized per atom), which characterizes the bond distribution over bonding pairs with an angle close to 180° [211]. As shown in Fig. 9c, upon melt-quenching, amorphous GeTe shows a strong correlation of short-long bond pattern (Peierls distortion) with a peak at 2.8/3.5 Å, while the ALTBC gets more centralized towards 3.3 Å in amorphous SnTe. In amorphous $Ge_1Sn_1Te_2$, the distorted GeTe bonds and undistorted SnTe bonds co-exist [192]. This difference in bonding pat-

tern is reminiscent of the behavior of their respective crystalline counterparts: GeTe forms a rhombohedral phase with strong Peierls distortion, while SnTe forms a perfect rocksalt structure with no Peierls distortion at room temperature.

The reduction in drift coefficient can be viewed as an increasing similarity in local bonding configuration between its amorphous and crystalline phases upon Sn alloying. This tuning, however, also reduces the energy barriers for crystallization, as reflected from the primitive rings analysis in that amorphous SnTe shows a much more ordered network than amorphous GeTe (Fig. 9d) [192]. Indeed, amorphous SnTe crystallizes spontaneously at room temperature. Nevertheless, short-term storage with low drift features over hours is already sufficient for most neuro-inspired computing tasks. It can be speculated that further engineering of $Ge_xSn_{1-x}Te$ towards Sn-rich compositions could help identify an optimized balance between ultralow drift (ν towards 0.005 and below) at room temperature, yet with rapid phase transition capability. Alternatively, it has been shown that light-element dopants, such as nitrogen (N), could also help reduce the drift coefficient of amorphous GeTe and GST to certain extent [241]. This behavior could be partly attributed to the formation of very short and strong N-Ge bonds (<2 Å), hindering the relaxation of Ge motifs in amorphous GeTe and GST [242].

Strategy III – Heterostructure design

The state-of-the-art PCM device can sustain more than 10^{12} cycles for binary storage [243]. However, resistance drift is exacerbated upon such extensive cycling. This happens because the material composition in the PCM cell already heavily fluctuates from location to location, well before device failure [244]. Post-mortem TEM experiments of GST memory cells provided direct evidence of elemental migration after extensive cycling, where voltage polarity effects were clearly observed: Sb/Ge atoms and Te atoms moved in an opposite direction [245]. This long-range transport eventually resulted in voids formation near the bottom electrode and elemental segregation, causing RESET-stuck and SET-stuck failures, respectively [244]. A typical degraded GST cell after trillions of cycles is shown in Fig. 10a [246]. The corresponding elemental mapping analysis clearly shows a Sb-enriched area near the top electrode, but a Sb-poor and Te-rich area near the bottom electrode (Fig. 10b). Such phenomenon stems from the negligible charge transfer between the cation-like Sb/Ge atoms and the anion-like Te atoms, which is evidenced by the calculated Bader charges for amorphous GST [226]. As shown in Fig. 10c, each data point corresponds to the degree of charge transfer of one specific atom. This particular amorphous model contains 60 Ge, 60 Sb and 150 Te atoms, as indicated by the red, black and blue data points in Fig. 10c. The Bader change analysis was made based on a static structural snapshot at zero K, which could reveal the direction of electromigration. Moreover, it was shown in a more recent work [247] that the magnitude of electromigration could also be assessed by calculating the effective (dynamical) charges of liquid PCMs within a nonequilibrium Green's function method based on DFT. In Ref. [246], it was demonstrated that by reversing the voltage polarity, backward elemental migration, termed as device self-healing, can be accomplished [246]. As shown in Fig. 10d, by sending RESET
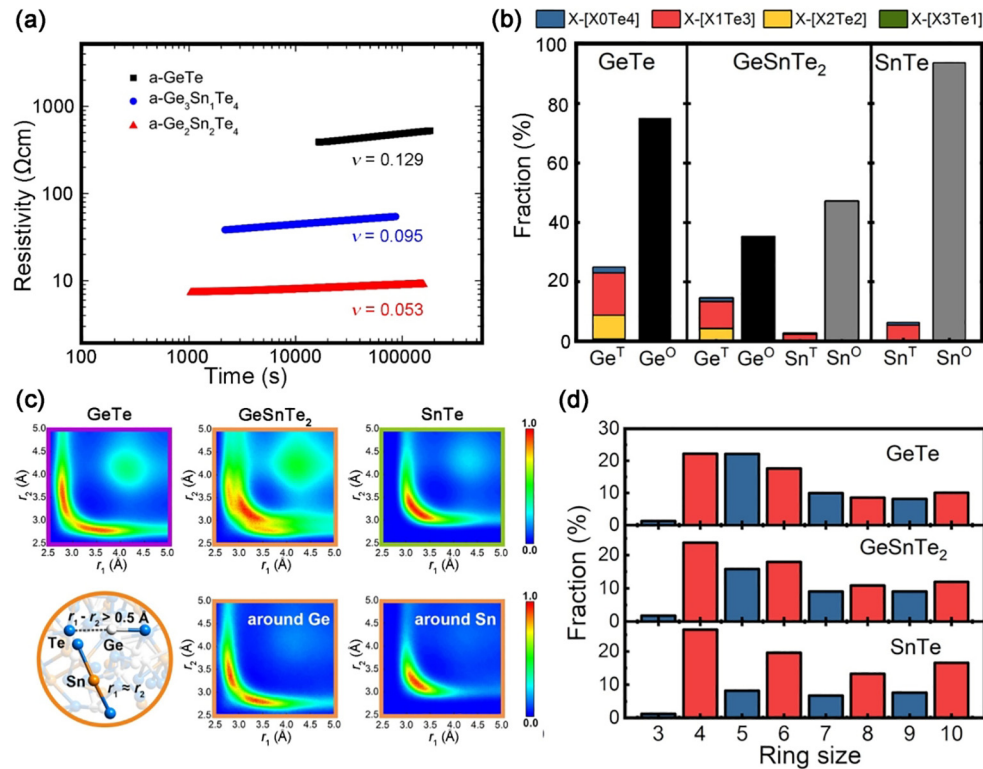
FIGURE 9

Drift suppression in amorphous $Ge_xSn_{1-x}Te$ alloys. (a) The drift coefficients ν measured at 50 °C for amorphous GeTe, $Ge_3Sn_1Te_4$ and $Ge_1Sn_1Te_2$ thin films are 0.129, 0.095 and 0.053, respectively. (b) The fraction of tetrahedral and defective octahedral motifs in melt-quenched amorphous GeTe, $Ge_1Sn_1Te_2$ and SnTe models. For all three amorphous models, the tetrahedral units are stabilized by homopolar bonds. (c) The degree of Peierls distortion evaluated by angular-limited three-body correlation (ALTBC) for the three amorphous models. The detailed atomic model and element-resolved ALTBCs of amorphous $Ge_1Sn_1Te_2$ are also shown. (d) Primitive rings analysis of the three amorphous models. Panel (a) is adapted with permission from Ref. [240], AIP. Panels (b)–(d) are adapted with permission from Ref. [192], RSC.

voltage pulses with reversed polarity, the large void shrinks gradually, as indicated by the red arrows. During this self-healing process, the cell resistance remains very high (open circles in Fig. 10e). The healed cell can be further switched between different resistance states, as indicated by the red and black points shown in Fig. 10e.

The self-healing programming scheme is an effective approach in extending the cycling endurance of PCM devices. However, the atomic transport of the charged cation-like and anion-like atoms proceeds with increasing cycle. Given the steadily increasing difference in elemental distribution and potential phase segregation, the structural relaxation path of amorphous GST becomes much more complex. In other words, aging is now not only caused by structural evolution at a fixed alloy composition, but also by time-dependent redistribution of constituent elements from one place to another. Major variations of resistance are expected to result from the temporally and spatially changed composition. Therefore, a general solution that prevents long-range elemental migration is needed, to ward off the compositional variation and random fluctuation. This goal has been achieved recently in Ref. [248] by constructing a heterostructure framework, termed as phase-change heterostructure (PCH). The conventional PCM-based and the new PCH-based device setups are compared in Fig. 11a and b. To suppress the long-distance atomic transport along the pulsing direction,

multiple layers of non-phase-change confinement crystal divide the PCM into nanolayers. This effectively confines atomic diffusion in the PCM fragments. The confinement crystal to compartmentalize the PCM is carefully chosen so as to have comparable electrical resistivity, larger thermal resistivity, much smaller lattice parameter, stronger chemical bonds, higher melting temperature with respect to the PCM. In addition, the confinement crystal should be feasible for co-sputtering and preferentially weakly coupled with PCM. Transition metal dichalcogenides (TMDC) [249–251] are suitable choices, and the combination of $TiTe_2$ and Sb_2Te_3 were demonstrated to be a robust material combination to implement the PCH idea [248].

The crystal structures of $TiTe_2$ and Sb_2Te_3 are shown in Fig. 11c and d. The former crystal has a much smaller lattice parameter 3.77 Å as compared to the latter 4.26 Å. The COHP bonding analysis also confirms that $TiTe_2$ to be chemically more robust than the Sb_2Te_3. The two crystals are alternately stacked up and are heated to very high temperature by using AIMD simulations, and after tens of ps, the Sb_2Te_3 nanolayers are fully melted while the $TiTe_2$ nanolayers retain in the crystalline form. The dynamics and mobility of Sb and Te atoms undergo a rapid decay from the middle of the PCM slab towards to interface region, and atoms bounce back if they get too close to the $TiTe_2$ crystal (Fig. 11e). Rapid cooling of the PCH model to room T results in a stable configuration of $TiTe_2$ crystal and Sb_2Te_3 glass.
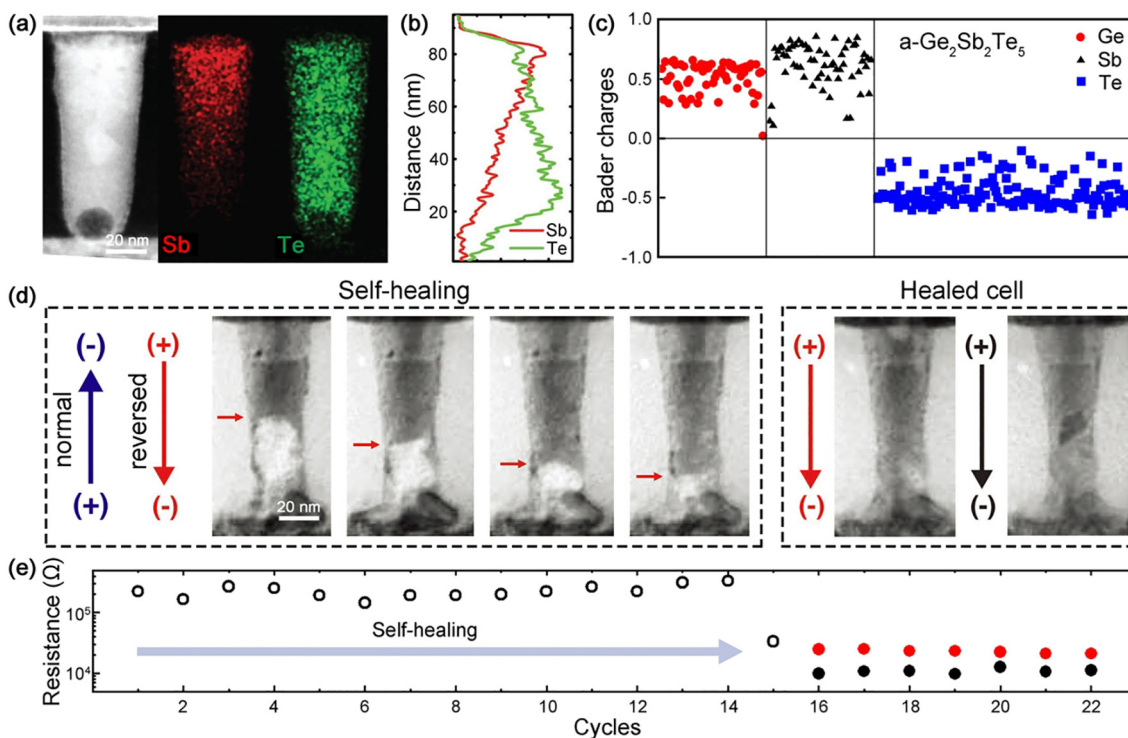
FIGURE 10

Elemental migration induced device failure. (a) TEM characterization and energy dispersive X-ray spectroscopy (EDX) mapping of a failed GST device. A big void is found near the bottom electrode. (b) Intensity profile of Sb and Te from the EDX mapping along the vertical pulsing direction, quantifying the inhomogeneous elemental distribution after device failure. (c) Bader charges calculated based on an AIMD generated amorphous GST model, which quantify the degree of charge transfer between Ge/Sb and Te atoms. (d) In situ TEM observation of self-healing process with multiple RESET pulses of reversed polarity. The large void is gradually healed, as indicated by the red arrows. The healed cell is then programmed using a RESET pulse and a SET pulse. (e) The cell resistance remains high during the self-healing programming, as indicated by the open circles. The healed cell can be switched between different resistance levels, as indicated by the red and black points. Panels (a), (b) and (d) are adapted with permission from Ref. [246], Wiley-VCH. Panel (c) is adapted with permission from Ref. [226], IOP.
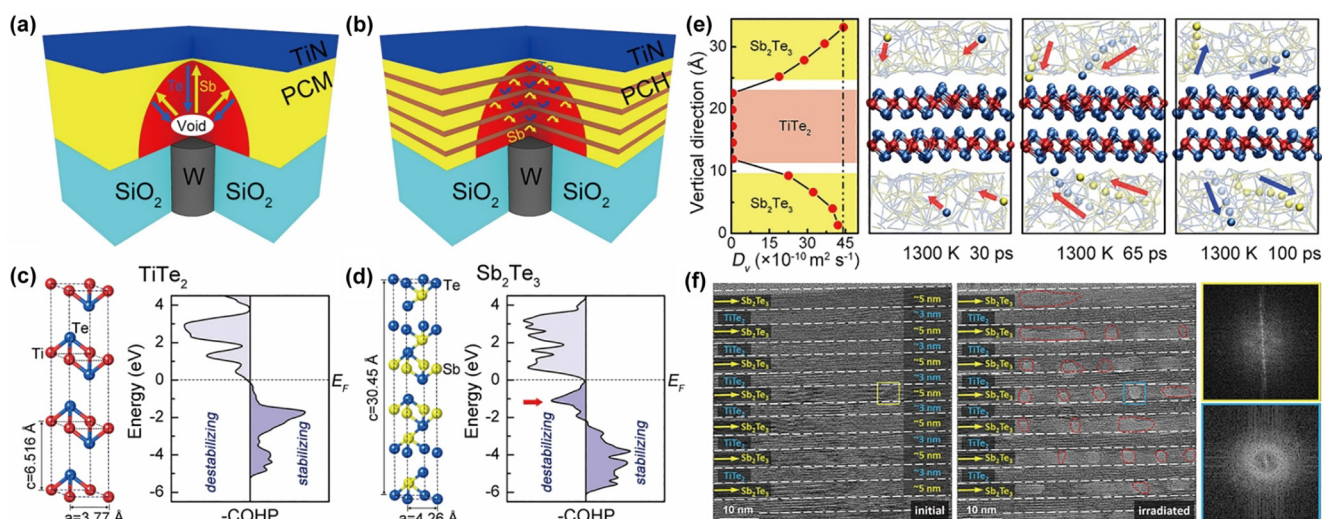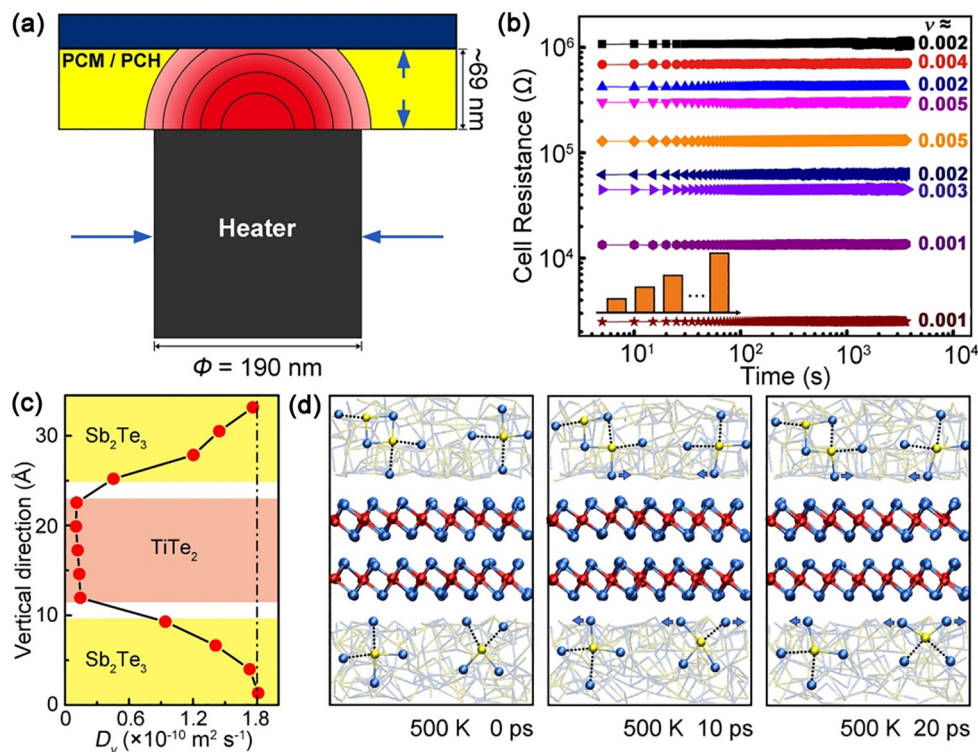

FIGURE 11

Concept of phase-change heterostructure (PCH). (a) and (b) The sketch of a PCM cell and a PCH cell. The device setup is the same and the only difference comes from sputtering of PCM or co-sputtering of PCH. (c) and (d) The crystal structures and COHP bonding analysis of $TiTe_2$ and Sb_2Te_3. An antibonding interaction appears in Sb_2Te_3 right below the Fermi level, while $TiTe_2$ shows bonding interactions for all occupied energy bands. (e) AIMD simulation of a $TiTe_2/Sb_2Te_3$ PCH model at very high temperatures. The PCM part is quickly melted, while the confinement material retains its crystalline form, showing good dynamically stability. A few Sb and Te atoms are highlighted in the PCM slab, while others are indicated by semitransparent Sb-Te bonds. Ti, Sb and Te atoms are rendered with red, yellow and blue spheres, respectively. (f) In situ TEM experiments performed on a $TiTe_2/Sb_2Te_3$ PCH thin film. The extensive electron beam irradiation triggered amorphization in the PCM nanolayers, but the confinement nanolayers remained robust. Adapted with permission from Ref. [248], AAAS.

More direct evidence of this confined phase transition scheme is provided by *in situ* TEM experiments carried out on $TiTe_2/Sb_2Te_3$ thin films. Upon extensive electron beam irradiation [252], progressive amorphization takes place in the Sb_2Te_3 nanolayers but not in the $TiTe_2$ confinement nanolayers [248], as shown in Fig. 11f.

A PCH device was then fabricated, as sketched in Fig. 12a. The PCH was ~69 nm in total film thickness, with alternately and repeatedly grown Sb_2Te_3 (~5 nm) and $TiTe_2$ (~3 nm) nanolayers. After a 2.15 V and 20 ns RESET pulse, the PCH device shows an ultralow drift coefficient v ~0.002 at room temperature [248], which is a 55-fold reduction as compared to that of GST device, v ~0.11. By varying the pulse amplitude from 1.95 to 2.15 V while keeping the 20 ns fixed pulse width, the PCH device shows consistently low drift coefficients below v ~0.005 for 7 intermediate RESET states. Including the SET and RESET state, the PCH presents 9 robust resistance levels, as shown in Fig. 12b. In addition, the inter-cell variability is also sharply reduced in this constrained transition mode. The same iterative RESET operation was repeated over four additional PCH cells, and the multilevel resistance profiles showed only small relative standard deviations below 5.5%. Moreover, the PCH device shows more than 85% reduction in RESET energy, ultralow 1/f nose, high-consistency of progressive crystallization as well as extended cycling endurance [248]. Further engineering of the cell size, i.e. increase the PCH film thickness and decrease the diameter of bottom electrode heater (as indicated by arrows in Fig. 12a), could result in more intermediate resistance states. Overall, the PCH design provides an ideal material solution for multilevel data storage and neuro-inspired computing of high accuracies and consistencies, and can be readily incorporated into the mature device setups for production.

This strongly suppressed resistance drift phenomenon in PCH devices can be understood from three aspects. First, the amorphous Sb_2Te_3 PCM part no longer has Ge and tetrahedral defects, as shown by AIMD simulations. This switch in chemistry eliminated the motivation for structural relaxation, in the same vein as the composition tuning in Strategy II earlier. Second, the long-range diffusion induced compositional variation of amorphous Sb_2Te_3 is suppressed by the $TiTe_2$ nanoconfinement layers. The calculated dynamical diffusion profile of supercooled Sb_2Te_3 liquids shows a rapid decay at 500 K (Fig. 12c). Third, the reinforcement of Peierls distortion could become a driving force for aging in amorphous Sb_2Te_3, but this cannot happen vertically as shown by the detailed atomic arrangement in Fig. 12d. An increase in Peierls distortion is prohibited because $TiTe_2$ crystal is already chemically saturated, and does not chemically react with the amorphous atoms from the Sb_2Te_3 slab. When atoms, in particular Te atoms, get too close to the $TiTe_2$ walls, they will be distorted and repositioned along the planar directions, as indicated by Fig. 12d. The spatial gaps between the $TiTe_2$ walls and the Sb_2Te_3 nanolayers are therefore consistently retained in

FIGURE 12

Ultralow resistance drift in PCH devices. (a) Sketch of the PCH device. (b) Starting from the SET state, RESET pulses with a varied amplitude from 1.95 to 2.15 V but a fixed pulse width 20 ns were sent to the PCH device, which resulted in consistently low drift coefficients $v < $ ~0.005 for all the 9 resistance states at room T. (c) and (d) The diffusion profile and dynamical configurations in the PCH model at 500 K. The Sb-Te bonding pairs that represent a prohibited Peierls distortion are highlighted. The atomic positions of other Sb and Te atoms are indicated by semitransparent Sb-Te bonds. Ti, Sb and Te atoms are rendered with red, yellow and blue spheres, respectively. Adapted with permission from Ref. [248], AAAS.

supercooled liquid and amorphous state at low temperatures [248]. The reduction of resistance drift due to confinement effects is further supported by a direct comparison between thick and thin amorphous Sb_2Te_3 nanolayers, as discussed in the next section.

Strategy IV – Nanoconfined PCM

Taking a cue from Strategy III, it seems likely that a single PCM layer of a few nm thickness can by itself be a feasible strategy to suppress drift. Several factors point to the merits of this approach. First, the move towards nanoconfined PCM is in line with the trend of device miniaturization, an effective route to increase the bit density in industry. The current PCM cell size ranges from several tens to several hundreds of nanometers. With further fabrication efforts, it is feasible to scale down the cell size to just a few nm. It has been shown that PCM still functions well at a length scale of ~1.3 nm in a highly confined geometry [253]. Second, the nanoconfined PCM layer needs to be held in place by other materials, such that the PCM is in fact confined and affected by these materials in contact, which may slow down the relaxation kinetics, making it less conducive to structural relaxation and drift. Third, several studies on PCM nanoparticles have shown that the crystallization temperature (i.e., the stability of the amorphous state) increases as the size of the nanoparticles decreases, thus implying better thermal stability in confined geometries [141]. Fourth, the ultrascaled devices with strong confinement effects open a new opportunity to explore the potential uses of amorphous PCMs that are otherwise low in stability.

In Ref. [248], a ~5 nm Sb_2Te_3 thin film was deposited on a SiO_2 substrate by magnetron sputtering, and was capped with another SiO_2 layer. The TEM image and the corresponding electron diffraction pattern verify that the Sb_2Te_3 thin film is in the amorphous phase, as no crystalline order can be observed, even after several days after deposition (Fig. 13a). It should be noted that sub-micrometer-thick Sb_2Te_3 films get already partially crystallized in the as-sputtered deposit because of its low crystallization temperature of 85 °C [254]. The measured sheet resistance of the Sb_2Te_3 thin film shows a very low drift coefficient v ~0.005 at room temperature, as displayed in Fig. 13b. This is in stark contrast with a ~150-nm-thick Sb_2Te_3, for which the RESET amorphous state shows a much larger drift coefficient v ~0.066. The drift and aging of the ~5 nm Sb_2Te_3 thin film is in fact much more similar to the PCH device with multiple confined ~5 nm Sb_2Te_3 nanolayers discussed in Strategy III, but nowhere close to the ~150-nm-thick Sb_2Te_3 device [248]. This observation unambiguously demonstrates the effectiveness of nanosized amorphous PCM against resistance drift. It is actually possible that the amorphous PCM itself, even when free-standing in the absence of confinements, becomes less prone to structural relaxation when having nanoscale dimensions [255]. The underlying mechanism in this case, however, is yet to be understood.

When it comes to exploiting unstable amorphous PCMs, Strategy IV recently enabled the use of a single element, Sb, for phase-change applications [256–258]. Amorphous Sb is highly unstable and crystallizes spontaneously at room temperature, but it could be stabilized by nanoconfinement effects (Fig. 14a). In Ref. [256], an ultrascaled phase-change device was demonstrated, in which the thickness of PCM layer was scaled down to a few nm (Fig. 14b). For a 10-nm-thick Sb device, it is not feasible to retain the amorphous state at room temperature after RESET operation. However, if the Sb film thickness is down to 5 nm and below, the melt-quenched amorphous Sb can exist up to 50.8 hours at 20 °C (Fig. 14c). In a separate work [257], it was shown that ~4 nm-thick amorphous Sb thin film, sandwiched by SiO_2 layers, can be directly obtained upon sputtering, similar to that of amorphous Sb_2Te_3 discussed above. A low drift coefficient v ~0.003 was achieved in the amorphous Sb thin film. In a lateral device, the ~4 nm-thick RESET amorphous Sb layer confined by SiO_2 and TiN layers shows even better non-volatile features, with a 10-year data retention temperature of ~48 °C. Moreover, upon iterative RESET operation, 9 robust resistance states were achieved over 1000 s, with relatively small drift coefficients ranging from 0.006 to 0.027 at room T [257]. Taking into account the rapid crystallization capability and the extremely simplified chemistry with no compositional fluctuation possible
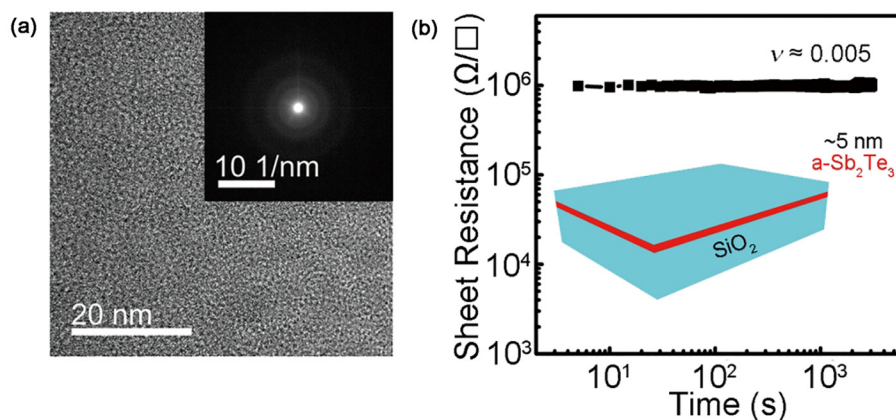
FIGURE 13

Nanometer amorphous Sb_2Te_3 thin films in confinement. (a) The sheet resistance measured for a ~5 nm thick sputtered amorphous Sb_2Te_3 thin film. The thin film was sandwiched between SiO_2 layers. The thin film shows a very low drift coefficient v ~0.005 at room temperature, similar to that of PCH device in Figure 12. (b) TEM image and electron diffraction pattern confirmed the confined Sb_2Te_3 thin film to be in a fully amorphous state. Adapted with permission from Ref. [248], AAAS.
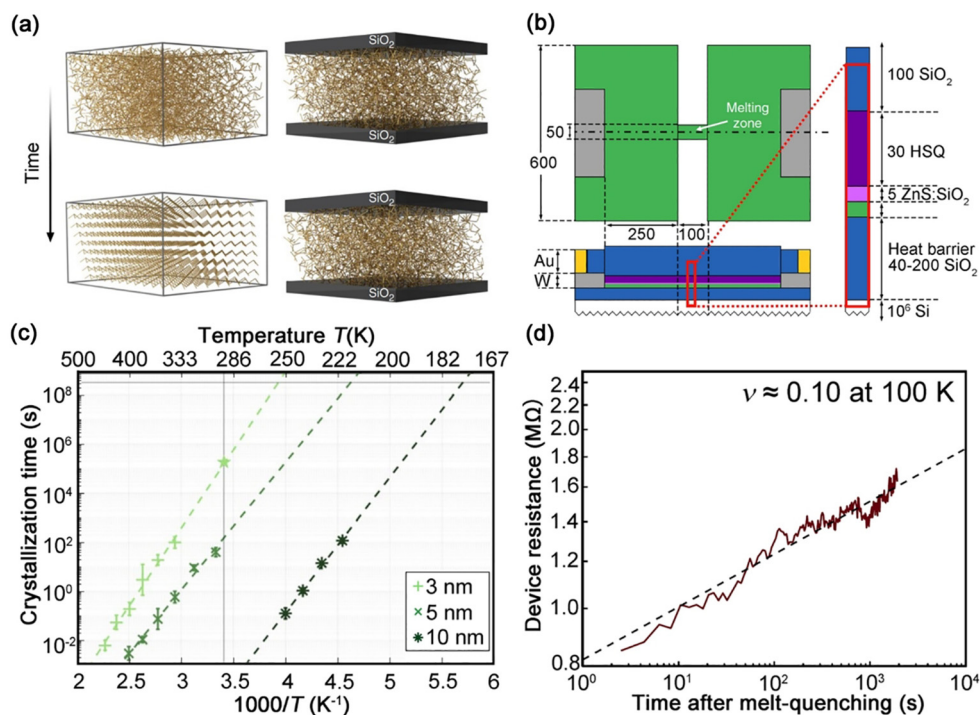
FIGURE 14

Nanoconfinement effects in single-element Sb-based device. (a) A miniaturized device with only ∼5 nm thick Sb thin film, in which amorphous Sb can be obtained in melt-quench. (b) Sketch of nanoconfinement. For a bulk Sb, the amorphous phase crystallizes spontaneously at room T, while the amorphous Sb thin film of a few nm thickness can retain its glassy structure at room T for hours under SiO$_2$ confinement. (c) The life time of melt-quenched amorphous Sb in devices measured at different temperatures. (d) The device resistance of RESET state measured at 100 K. Amorphous Sb shows a clear resistance drift with a coefficient v ∼0.10 at 100 K, similar to that of amorphous GST at room T. Panels (a) and (b)–(d) are adapted with permission from Ref. [258] and Ref. [256], Springer Nature limited.

upon programming, Sb is considered to be a very good candidate for practical memory and computing applications. Nevertheless, the detailed stabilization mechanisms of the nanoconfinement remain to be further explored. In particular, it is important to investigate the detailed relaxation path of amorphous Sb and Sb$_2$Te$_3$ at even lower temperatures, especially since amorphous Sb was found to exhibit a large drift coefficient v ∼0.10 at 100 K [256], similar to that of amorphous GST at room temperature.

Theoretical advance—Machine-learning interatomic potentials

In this section, we comment on an important theoretical advance – the development and use of machine-learning (ML) interatomic potentials [259,260] that have enabled thorough studies of crystallization kinetics [261–264], thermal conductivity [265,266], as well as aging and mid-gap states [213,227] in GeTe and GST. Despite the important contributions made by DFT and AIMD simulations for PCM research, it is not feasible to carry out large-scale simulations with sufficient statistical sampling to assess certain physical properties and processes, due to the heavy computational loads. For instance, an AIMD simulation of 400+ atom GST over 1 ns would already take more than half a year real-world time of a high-performance supercomputer [189,190]. For MD simulations with classical potentials, the computing efficiencies can be drastically improved by several orders

of magnitude, but the complex interplay between different atomic environments in PCMs makes the construction of classical potentials very challenging. Although a Tersoff-based potential was fitted for amorphous GeTe [267], it is not likely to be applied in more complex situations with surface or interface effects. It is also not feasible for classical potentials to describe the interatomic interactions accurately when the chemical complexity involves three or more elements. ML potentials provide a promising solution to this conundrum with quasi-*ab initio* accuracy and an efficiency almost comparable to classical potentials for calculating some key properties.

Machine learning is a subfield of AI that provides a route for systems to automatically learn and improve from large datasets without being explicitly programmed. The fitting and use of ML-based interatomic potential is an important application of ML in materials research. ML potentials are a mathematical representation of 3N-dimensional potential-energy surface with total energy, interatomic force and spatial distribution of N atoms [259]. In contrast to classical potentials, ML potentials do not make prior assumptions about the mathematical form of interatomic interactions, but instead are "learned" from a large reference database. The detailed procedure is shown in Fig. 15a. First, a comprehensive database is created (commonly) through DFT and AIMD calculations performed on small atomic models. Second, a mathematical representation is used to incorporate the atomic structure into ML algorithm, referred as descriptor. Third, the regression or "learning" of ML models is performed through
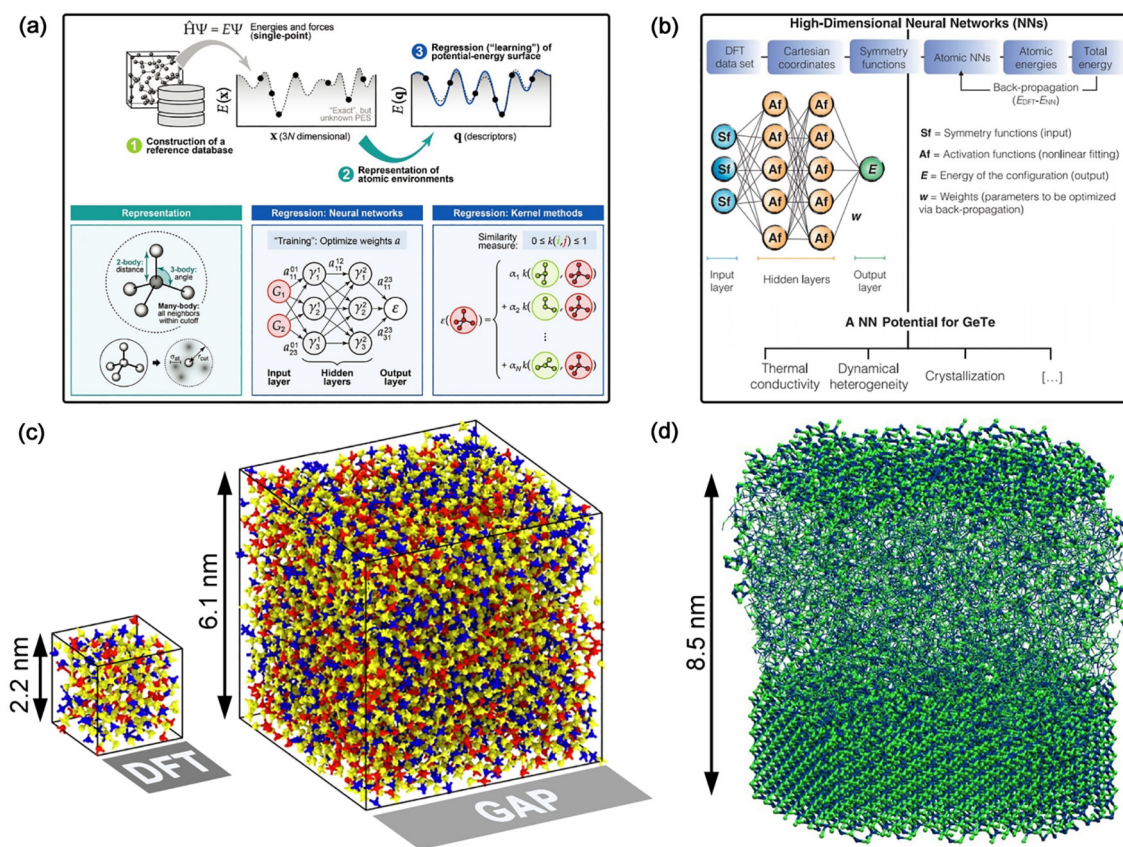
FIGURE 15

Machine-learning interatomic potentials. (a) The procedure to develop a neural network interatomic potential (NNP) for GeTe. The NNP is trained with respect to the AIMD data collected for small atomic models of a few hundreds of atoms. (b) General machine-learning methodology. In addition to NNP training, a Gaussian approximation potential (GAP) method based on the smooth overlap of atomic positions (SOAP) descriptors is addressed. (c) The NNP simulation of a GeTe nanowire with a partly amorphized fragment. The model contains 16,540 atoms in total with a diameter of ∼9 nm and a nanowire length of ∼8.5 nm. (d) The comparison of a small AIMD-based amorphous GST model, containing 315 atoms, and a large GAP-based amorphous GST model, containing 7200 atoms. Panel (a) is adapted with permission from Ref. [259], MRS. Panel (b) is adapted with permission from Ref. [269], Wiley-VCH. Panels (c) and (d) are adapted with permission from Ref. [228] and Ref. [271], ACS.

minimization of the difference in potential-energy surface with respect to the DFT-based one. Two descriptors, namely, atom-centered symmetry functions (ASCF) and smooth overlap of atomic positions (SOAP) have been used to characterize the atomic positions, bond length, bond angles and other structural features within a sphere of a cutoff radius ∼6 Å for amorphous PCMs (Fig. 15a and b). Larger cutoffs can be chosen to describe medium-range order. Two popular regression methods based on the neural-network and the Gaussian approximation approaches are typically adopted (Fig. 15a and b). Further technical details about these ML potentials can be found in recent reviews in Refs. [259,260].

The first neural-network potential (NNP) was proposed for GeTe in Ref. [268], which was extensively employed to study the crystallization kinetics, dynamical heterogeneity, thermal conductivity and the thermal-boundary resistance at the amorphous–crystalline interface [269]. Since the ML potentials cannot provide direct electronic information, DFT calculations are then used to conduct electronic structure calculations based on the amorphous structures produced by ML potentials. As discussed above, ML potentials were used in combination with metadynamics to assess the aging trend in amorphous GeTe [213]. More

recently, a Gaussian approximation potential (GAP) was developed for $Ge_2Sb_2Te_5$ in Ref. [228], allowing calculations of amorphous GST with thousands of atoms at a low computational cost (Fig. 15c). Melt-quenched amorphous GST models with up to 24,300 atoms have been calculated so far [270]. As mentioned earlier, sufficient statistical sampling over 30 independent melt-quench runs was made using GAP to assess the mid-gap states in amorphous GST [227]. Such potentials are promising to elucidate the potential aging paths in amorphous GST.

For both the NNP and GAP approaches, it is feasible to include surface or interface effects during the training of ML potentials. A partly amorphized GeTe nanowire model with 16,540 atoms is shown in Fig. 15d [271]. The amorphous part of the nanowire model shows a lower fraction of Ge-Ge chains than that in bulk amorphous GeTe, which could partly explain the reduced drift coefficient in nanowires [255]. We can foresee the rapid development of new ML potentials to study other PCMs, such as AIST, SST as well as pure Sb. The flexibility of the ML potentials could also take into account the environmental effects encountered in experiments and devices, which could enable thorough investigations on PCMs in nanowires, nanoparticles and other geometrical forms with strong confinements, such as encapsulated in

carbon nanotubes, as well as sandwiched by SiO_2, TiN and $TiTe_2$ layers. These models would come in handy, in an effort to probe into the nanoconfined PCM described in Strategy IV earlier.

The field of ML potentials is under very active development, benefiting fundamental research in many other materials systems [259,260]. But still the method has limitations, a primary one being that ML potentials are not transferrable, just like other classical potentials. One fitted potential can only be used for one chemical composition. If high pressure or surface/interface effects need to be considered for the specific composition, additional fitting and learning are compulsory. Besides, the accuracy of ML potentials largely depends on the quality of the training dataset. If the materials systems are not well characterized via DFT, such as strongly-correlated systems, then the trained potentials are also not accurate. Alternatively, it is also possible to construct ML potentials by training from existing experimental database. A few attempts have been made to predict the properties of some metallic glass [272], oxide glass [273] and silicate glass [274].

Outlook

In this review, we have summarized the progresses made towards a fundamental understanding of aging/relaxation in amorphous PCMs, and highlighted in particular its structural mechanisms at the atomic scale. We have also prescribed four strategies that can either bypass or suppress the aging induced resistance drift for practical implementations in PCM devices, based on their promising performance so far. Clearly, the accumulated structural understanding has led to innovative schemes to control the resistance drift. Taken together, these recent advances have laid a solid foundation for future development of PCM-based memory and computing devices towards ultrahigh storage density and programming accuracies and efficiencies at low volume cost.

In the preceding sections, we have already mentioned some unresolved questions along the way. Here as an outlook, we briefly point out a few more remaining challenges in the aging studies of amorphous PCMs. These issues are interesting for further research, with potential impact on applications. First, while the aging studies in amorphous GeTe and GST have shed light on the structural evolution underlying the aging-induced resistance drift, no universal picture is yet provided for aging in all PCMs, as the mechanism may depend on materials composition, doping elements and sample preparation methods. Second, the understanding of ultrascaled PCM and associated confinement effects on relaxation is only in its rudimentary stage, especially since their mechanisms and efficacy are dependent not only on the PCM material but also on the surrounding materials, and even on the configuration of the device set-up. The complexity associated with nanoconfinement is obvious, as we have already pointed out when invoking it in Strategies III and IV earlier. Third, the structural evolution is expected to have strong dependence on temperature and pressure conditions, which change both the thermal dynamic driving force and the kinetic pathways. The PCM properties are in fact known to be sensitive to both thermodynamic parameters. Fourth, the effects of aging on the subsequent crystallization kinetics remain to be further

explored. It is so far uncertain if the crystallization energy barrier is reduced or increased after relaxation in the amorphous structure. Furthermore, there has been no report about how the resistance changes upon aging when the amorphous state is subjected to a complex train of voltage pulses for neuro-inspired computing applications - the scenario most demanding on programming accuracies and consistencies of a PCM memory array.

Structural rejuvenation can be singled out as an interesting subject, as it offers another knob to turn to tweak the amorphous structure of PCMs. In fact, rejuvenation represents the opposite direction to relaxation in the evolution of glass structure, driving the glass towards a higher energy state. In other glass systems, such as metallic glasses, rejuvenation has been achieved thermally by heating to above the glass transition temperature or driven externally via mechanical deformation [275,276]. An extreme example is that shock compression can rejuvenate metallic glasses within hundreds of nanoseconds [277], a time scale relevant to memory and computing applications. Similar approaches may be adopted for rejuvenation studies in PCMs, which have so far been rather limited. There have been much studies on pressure induced amorphization and amorphous-amorphous transition in the PCMs [278–281], but their temporal electrical responses are not yet thoroughly investigated. In addition, the displacement forces induced by ion beam or extensive electron beam irradiation can result in direct amorphization of PCM crystal [252,282], which could in principle lead to higher energy amorphous states. Further experimental and simulation efforts are needed to study rejuvenation and the subsequent aging of amorphous PCMs. It is conceivable that resistance drift can be reversed upon rejuvenation.

An important property of amorphous PCMs and other (closely related) chalcogenide glasses is the Ovonic threshold switching (OTS) phenomenon [238], which has been exploited for projected memory implementation discussed above [236]. In contrast to memory switching, OTS is a volatile transition. As the external voltage increases, the resistance of the amorphous state suddenly drops by several orders of magnitude over a time span on picoseconds level, but still retain its amorphous structure, termed as amorphous ON state. If the voltage is removed, then the resistance returns to its initial value. It is a very interesting question whether structural rearrangement in the amorphous phase plays a role in OTS switching and whether aging in the amorphous phase affects the barrier of OTS switching. A couple of mechanisms have been proposed to account for OTS transition [283], including thermal runaway [284], field-induced nucleation [285] and generation and recombination of charge carriers [286]. A very recent paper claims that OTS transition involves the metastable formation of newly introduced metavalent bonds under electric field in amorphous germanium-(antimony)-selenides [287]. Nevertheless, the accumulated knowledge for OTS has not yet enabled the design and synthesis of an ultimate OTS material as selectors to be integrated with PCM cells in the 3D X point architecture.

Besides electrical contrast, the phase transition between the amorphous and crystalline states also accompanies a strong change in optical reflectivity [2]. The switching between the two states can be accomplished by laser pulses. In fact, PCMs

were firstly used as rewritable optical compact discs, digital versatile discs and Blu-ray discs [2]. In recent years, the integration with silicon waveguides render PCM an excellent candidate for non-volatile applications [288,289]. In addition to non-volatile photonic binary and multilevel memory [290–292], arithmetic and logic processing [293,294], as well as synaptic and neuronal mimics [295,296], PCM can also be exploited to develop flexible and rollable displays with nanopixel resolution [297], to create metamaterials [298], to confine surface phonon polaritons [299] and to serve as switches and routers in emerging quantum computing and telecommunication architectures [300]. Structural relaxation of the amorphous state also leads to a drift in optical reflectance, yet the issue is less serious in photonic applications, therefore is far less addressed so far. Nevertheless, new PCMs discussed in the strategies in the preceding section, such as Sc-Sb-Te alloys with ultrafast nucleation capacity, ultrathin Sb, and $TiTe_2/Sb_2Te_3$ heterostructure with ultralow drift and noise features, offer promising new candidates to be explored for photonic PCM applications.

Declaration of Competing Interest

The authors declare that they have no known competing financial interests or personal relationships that could have appeared to influence the work reported in this paper.

Acknowledgments

References

[1] W. Zhang et al., Nat. Rev. Mater. 4 (2019) 150.
[2] M. Wuttig, N. Yamada, Nat. Mater. 6 (2007) 824.
[3] W. Zhang et al., MRS Bull. 44 (2019) 686.
[4] W. Welnic, M. Wuttig, Mater. Today 11 (2008) 20.
[5] D. Ielmini, A.L. Lacaita, Mater. Today 14 (2011) 600.
[6] S. Raoux et al., Chem. Rev. 110 (2010) 240.
[7] H.-S.-P. Wong et al., Proc. IEEE 98 (2010) 2201.
[8] P. Fantini, J. Phys. D: Appl. Phys. 53 (2020) 283002.
[9] Y. Wang et al., Mater. Today 28 (2019) 63.
[10] Y. Yang, R. Huang, Nat. Electron. 1 (2018) 274.
[11] S. Liu et al., Adv. Mater. 28 (2016) 10623.
[12] P. Yao et al., Nature 577 (2020) 641.
[13] S. Mangin et al., Nat. Mater. 5 (2006) 210.
[14] J. Torrejon et al., Nature 547 (2017) 428.
[15] S. Bhatti et al., Mater. Today 20 (2017) 530.
[16] A. Chanthbouala et al., Nat. Mater. 11 (2012) 860.
[17] R. Berdan et al., Nat. Electron. 3 (2020) 259.
[18] L. Chen et al., Nanoscale 10 (2018) 15826.
[19] Y. van de Burgt et al., Nat. Mater. 16 (2017) 414.
[20] J. Rivnay et al., Nat. Rev. Mater. 3 (2018) 17086.
[21] Y. van de Burgt et al., Nat. Electron. 1 (2018) 386.
[22] E.J. Yoo et al., Adv. Mater. 27 (2015) 6170.
[23] K. Kang et al., Adv. Mater. 31 (2019) 1804841.
[24] Z. Lv et al., Chem. Rev. 120 (2020) 3941.
[25] Y. Shi et al., Nat. Electron. 1 (2018) 458.
[26] M. Wang et al., Nat. Electron. 1 (2018) 130.
[27] C. Liu et al., Nat. Nanotechnol. 13 (2018) 404.
[28] R. Yang et al., Nat. Electron. 2 (2019) 108.
[29] F. Zhou et al., Research 2019 (2019) 9490413.
[30] C.S. Yang et al., Adv. Mater. 29 (2017) 1700906.
[31] Z. Zhang et al., InfoMat 2 (2020) 261.
[32] F. Rao et al., Science 358 (2017) 1423.
[33] B. Chen et al., Chem. Mater. 31 (2019) 8794.
[34] G.M. Zewdie et al., Chem. Mater. 31 (2019) 4008.
[35] D. Loke et al., Science 336 (2012) 1566.
[36] D.K. Loke et al., ACS Appl. Mater. Interfaces 10 (2018) 41855.
[37] J. Orava, A.L. Greer, Acta Mater. 139 (2017) 226.
[38] C.D. Wright et al., Adv. Mater. 23 (2011) 3408.
[39] D. Kuzum et al., Nano Lett. 12 (2012) 2179.
[40] C.D. Wright et al., Adv. Funct. Mater. 23 (2013) 2248.
[41] G.W. Burr et al., Adv. Phys. X 2 (2016) 89.
[42] T. Tuma et al., Nat. Nanotechnol. 11 (2016) 693.
[43] C.D. Wright, Nat. Nanotechnol. 11 (2016) 655.
[44] S. Ambrogio et al., Front. Neurosci. 10 (2016) 56.
[45] A. Sebastian et al., Nat. Commun. 8 (2017) 1115.
[46] N. Gong et al., Nat. Commun. 9 (2018) 2102.
[47] I. Boybat et al., Nat. Commun. 9 (2018) 2514.
[48] A. Pantazi et al., Nanotechnology 27 (2016) 355205.
[49] A. Sebastian et al., J. Appl. Phys. 124 (2018) 111101.
[50] D. Ielmini, H.-S.-P. Wong, Nat. Electron. 1 (2018) 333.
[51] A. Sebastian et al., Nat. Nanotechnol. 15 (2020) 529.
[52] N. YamadaJpn et al., J. Appl. Phys. Part 1 (26) (1987) 61.
[53] N. Yamada, T. Matsunaga, J. Appl. Phys. 88 (2000) 7020.
[54] T. Matsunaga et al., Acta Crystallogr., B 60 (2004) 685.
[55] M. Chen et al., Appl. Phys. Lett. 49 (1986) 502.
[56] G. Bruns et al., Appl. Phys. Lett. 95 (2009) 043108.
[57] R. Wang et al., NPG Asia Mater. 9 (2017) e396.
[58] J.E. Boschker et al., CrystEngComm 19 (2017) 5324.
[59] T. Matsunaga, N. Yamada, Phys. Rev. B 69 (2004) 104111.
[60] P. Jóvári et al., Phys. Rev. B 77 (2008) 035202.
[61] B. Sa et al., PCCP 12 (2010) 1585.
[62] M. Krbal et al., Phys. Rev. B 84 (2011) 104106.
[63] H.Y. Cheng et al., IEDM Technol. Dig. (2011) 3.4.1.
[64] M. Agati et al., J. Mater. Chem. C 7 (2019) 8720.
[65] F. Arnaud et al., IEDM Technol. Dig. (2018) 18.4.1.
[66] P. Cappelletti et al., J. Phys. D Appl. Phys. 53 (2020) 193002.
[67] M. Zhu et al., Nat. Commun. 5 (2014) 4086.
[68] F. Rao et al., Nat. Commun. 6 (2015) 10040.
[69] Z. Li et al., ACS Appl. Mater. Interfaces 8 (2016) 26126.
[70] B. Liu et al., ACS Appl. Mater. Interfaces 12 (2020) 20672.
[71] L. Peng et al., J. Alloy. Compd. 821 (2020) 153499.
[72] Z. Li et al., J. Appl. Phys. 122 (2017) 195107.
[73] S. Hu et al., J. Mater. Chem. C 8 (2020) 6672.
[74] C. Qiao et al., Appl. Phys. Lett. 114 (2019) 071901.
[75] S. Hu et al., Comput. Mater. Sci. 165 (2019) 51.
[76] X.-P. Wang et al., NPJ Comput. Mater. 6 (2020) 31.
[77] Y. Zhou et al., J. Mater. Chem. C 8 (2020) 3646.
[78] H. IwasakiJpn. et al., J. Appl. Phys. Part 1 (32) (1993) 5241.
[79] L. van Pieterson et al., J. Appl. Phys. 97 (2005) 083520.
[80] M.H.R. Lankhorst et al., Nat. Mater. 4 (2005) 347.
[81] T. Matsunaga et al., Nat. Mater. 10 (2011) 129.
[82] M. Zhu et al., Nat. Commun. 10 (2019) 3525.
[83] M. Salinga et al., Nat. Commun. 4 (2013) 2371.
[84] P. Zalden et al., J. Appl. Phys. 107 (2010) 104312.
[85] I. Ronneberger et al., Phys. Status Solidi RRL 13 (2019) 1800552.
[86] M. Xu et al., PCCP 21 (2019) 4494.
[87] D. Silver et al., Nature 529 (2016) 484.
[88] Y. Zhang et al., Appl. Phys. Rev. 7 (2020) 011308.
[89] N. Yamada et al., J. Appl. Phys. 69 (1991) 2849.
[90] A.L. Greer, Nat. Mater. 14 (2015) 542.
[91] S. Wei et al., Phys. Rev. Appl. 7 (2017) 034035.
[92] H. Weber et al., Phys. Rev. Mater. 2 (2018) 093405.
[93] E. Morales-Sánchez et al., J. Appl. Phys. 91 (2002) 697.
[94] J. Kalb et al., J. Mater. Res. 22 (2007) 748.
[95] J.-Y. Cho et al., Acta Mater. 94 (2015) 143.
[96] B. Chen et al., J. Phys. Chem. C 121 (2017) 8569.
[97] J. Pries et al., Adv. Mater. 31 (2019) 1900784.
[98] A. Pirovano et al., IEEE Trans. Electron. Dev. 51 (2004) 714.
[99] A. Redaelli et al., IEEE Electron. Dev. Lett. 25 (2004) 684.
[100] P. Fantini et al., Appl. Phys. Lett. 88 (2006) 263506.
[101] D. Ielmini et al., IEEE Trans. Electron. Dev. 54 (2007) 308.
[102] I.V. Karpov et al., J. Appl. Phys. 102 (2007) 124503.
[103] D. Ielmini, M. Bonardi, Appl. Phys. Lett. 94 (2009) 091906.

[104] M. Boniardi et al., J. Appl. Phys. 105 (2009) 084506.
[105] M. Boniardi et al., IEEE Trans. Electron. Dev. 57 (2010) 2690.
[106] M. Boniardi, D. Ielmini, Appl. Phys. Lett. 98 (2011) 243506.
[107] M. Rizzi et al., Appl. Phys. Lett. 99 (2011) 223513.
[108] P. Fantini et al., Appl. Phys. Lett. 100 (2012) 213506.
[109] P. Fantini et al., Appl. Phys. Lett. 102 (2013) 253505.
[110] M. Rutten et al., Sci. Rep. 5 (2015) 17362.
[111] M.L. Gallo et al., Adv. Electron. Mater. 4 (2018) 1700627.
[112] P. Noé et al., Semicond. Sci. Technol. 33 (2018) 013002.
[113] D. Ielmini et al., Appl. Phys. Lett. 92 (2008).
[114] J.-Y. Raty, Phys. Status Solidi RRL 13 (2019) 1800590.
[115] B. Kersting et al., Sci. Rep. 10 (2020) 8248.
[116] S.R. Elliott, J. Phys. D Appl. Phys. 53 (2020) 214002.
[117] G.W. Burr et al., IEEE J. EM. Sel. Top. C. 6 (2016) 146.
[118] A. Sebastian et al., J. Phys. D Appl. Phys. 52 (2019) 443002.
[119] M. Le Gallo, A. Sebastian, J. Phys. D Appl. Phys. 53 (2020) 213002.
[120] J. Orava et al., Nat. Mater. 11 (2012) 279.
[121] J. Orava et al., Adv. Funct. Mater. 25 (2015) 4851.
[122] P. Zalden et al., Science 364 (2019) 1062.
[123] F. Rao et al., Science 364 (2019) 1032.
[124] J. Akola, R.O. Jones, Science 358 (2017) 1386.
[125] T.H. Lee, S.R. Elliott, Phys. Rev. Lett. 107 (2011) 145702.
[126] K. Shportko et al., Nat. Mater. 7 (2008) 653.
[127] D. Lencer et al., Nat. Mater. 7 (2008) 972.
[128] M. Zhu et al., Adv. Mater. 30 (2018) 1706735.
[129] M. Wuttig et al., Adv. Mater. 30 (2018) 1803777.
[130] T. Siegrist et al., Nat. Mater. 10 (2011) 202.
[131] W. Zhang et al., Nat. Mater. 11 (2012) 952.
[132] P. Jost et al., Adv. Funct. Mater. 25 (2015) 6399.
[133] W. Zhang et al., Sci. Rep. 5 (2015) 13496.
[134] P. Nukala et al., Nano Lett. 14 (2014) 2201.
[135] T.-T. Jiang et al., Acta Mater. 187 (2020) 103.
[136] R.E. Simpson et al., Nat. Nanotechnol. 6 (2011) 501.
[137] B. Sa et al., Phys. Rev. Lett. 109 (2012) 096802.
[138] J. Tominaga et al., Adv. Mater. Inter. 1 (2014) 1300027.
[139] J. Momand et al., Nanoscale 7 (2015) 19136.
[140] J.-J. Wang et al., Chem. Mater. 30 (2018) 4770.
[141] B.J. Kooi, M. Wuttig, Adv. Mater. 32 (2020) 1908302.
[142] J. Pries et al., MRS Bull. 44 (2019) 699.
[143] S. Wei et al., MRS Bull. 44 (2019) 691.
[144] A. Lotnyk et al., Nanoscale Adv. 1 (2019) 3836.
[145] J.-J. Wang et al., Materials 10 (2017) 862.
[146] W. Zhang, M. Wuttig, Phys. Status Solidi RRL 13 (2019) 1900130.
[147] J. Tominaga, Phys. Status Solidi RRL 13 (2019) 1800539.
[148] Xian-Bin Li et al., Adv. Funct. Mater. 28 (2018) 1803380.
[149] M. Le Gallo et al., Nat. Electron. 1 (2018) 246.
[150] R.O. Jones, Rev. Mod. Phys. 87 (2015) 897.
[151] S. Caravati et al., Appl. Phys. Lett. 91 (2007) 171906.
[152] J. Akola, R.O. Jones, Phys. Rev. B 76 (2007) 235201.
[153] M. Xu et al., Phys. Rev. Lett. 103 (2009) 195502.
[154] R. Mazzarello et al., Phys. Rev. Lett. 104 (2010) 085503.
[155] S. Caravati et al., Phys. Rev. B 81 (2010) 014201.
[156] S. Caravati et al., J. Phys.: Condens. Matter 22 (2010) 315801.
[157] G.C. Sosso et al., Phys. Rev. B 83 (2011) 134201.
[158] S. Gabardi et al., J. Phys.: Condens. Matter 24 (2012) 385803.
[159] S. Gabardi et al., J. Chem. Phys. 144 (2016) 204508.
[160] J. Akola, R.O. Jones, Phys. Rev. Lett. 100 (2008) 205502.
[161] J. Akola et al., Phys. Rev. B 83 (2011) 094113.
[162] J. Akola, R.O. Jones, Appl. Phys. Lett. 94 (2009) 251905.
[163] J. Akola, R.O. Jones, Phys. Rev. B 79 (2009) 134118.
[164] J. Akola et al., Phys. Rev. B 80 (2009) 020201.
[165] J. Kalikka et al., J. Phys.: Condens. Matter 25 (2013) 115801.
[166] I. Voleská et al., Phys. Rev. B 86 (2012) 094108.
[167] M. Ropo et al., Phys. Rev. B 96 (2017) 184102.
[168] R.O. Jones et al., J. Chem. Phys. 146 (2017) 194502.
[169] R.O. Jones, Phys. Rev. B 101 (2020) 024103.
[170] X.-P. Wang et al., Acta Mater. 136 (2017) 242.
[171] M. Xu et al., J. Mater. Chem. C 8 (2020) 6364.
[172] M. Xu et al., J. Mater. Chem. C 7 (2019) 9025.
[173] C. Qiao et al., J. Mater. Chem. C 6 (2018) 5001.
[174] Y.-R. Guo et al., PCCP 20 (2018) 11768.
[175] X.-B. Li et al., Phys. Rev. Lett. 107 (2011) 015501.
[176] J. Hegedüs, S.R. Elliott, Nat. Mater. 7 (2008) 399.
[177] J.M. Skelton et al., J. Appl. Phys. 112 (2012) 064901.
[178] J.M. Skelton et al., Appl. Phys. Lett. 101 (2012) 024106.
[179] K. Konstantinou et al., J. Phys.: Condens. Matter 30 (2018) 455401.
[180] T.H. Lee, S.R. Elliott, Adv. Mater. 29 (2017) 1700814.
[181] W. Zhang et al., Chem. Month. 145 (2014) 97.
[182] W. Zhang et al., Adv. Mater. 24 (2012) 4387.
[183] K. Bai, Acta Mater. 181 (2019) 439.
[184] B. Cai et al., Appl. Phys. Lett. 97 (2010) 191908.
[185] B. Prasai et al., Phys. Stat. Sol. b 250 (2013) 1785.
[186] W. Zhang et al., MRS Bull. 40 (2015) 856.
[187] J. Kalikka et al., Phys. Rev. B 86 (2012) 144113.
[188] J. Kalikka et al., Phys. Rev. B 90 (2014) 184109.
[189] J. Kalikka et al., Phys. Rev. B 94 (2016) 134105.
[190] I. Ronneberger et al., Adv. Funct. Mater. 25 (2015) 6407.
[191] I. Ronneberger et al., MRS Comm. 8 (2018) 1018.
[192] Y. Chen et al., J. Mater. Chem. C 8 (2020) 71.
[193] T. Hughbanks, R. Hoffmann, J. Am. Chem. Soc. 105 (1983) 3528.
[194] R. Dronskowski, P.E. Blöchl, J. Phys. Chem. 97 (1993) 8617.
[195] V.L. Deringer et al., J. Phys. Chem. A 115 (2011) 5461.
[196] S. Maintz et al., J. Comput. Chem. 37 (2016) 1030.
[197] J. Luckas et al., J. Mater. Res. 28 (2013) 1139.
[198] C. Longeaud et al., J. Appl. Phys. 112 (2012) 113714.
[199] J. Luckas et al., J. Appl. Phys. 110 (2011) 013719.
[200] V.L. Deringer et al., Angew. Chem. Int. Ed. 53 (2014) 10817.
[201] A.V. Kolobov et al., Phys. Rev. B 87 (2013).
[202] A.V. Kolobov et al., Nat. Mater. 3 (2004) 703.
[203] S. Kohara et al., Appl. Phys. Lett. 89 (2006) 201910.
[204] D. Baker et al., Phys. Rev. Lett. 96 (2006) 255501.
[205] M.A. Paesler et al., J. Phys. Chem. Solids 68 (2007) 873.
[206] X.Q. Liu et al., Phys. Rev. Lett. 106 (2011) 025501.
[207] J.-Y. Raty et al., Phys. Rev. Lett. 108 (2012) 239601.
[208] P. Fons et al., Phys. Rev. Lett. 108 (2012) 239603.
[209] J. Wang et al., Nanoscale 10 (2018) 7363.
[210] J. Luckas, PhD thesis, RWTH Aachen (2012).
[211] J.-Y. Raty et al., Nat. Commun. 6 (2015) 7467.
[212] P. Fantini et al., Appl. Phys. Lett. 100 (2012) 013505.
[213] S. Gabardi et al., Phys. Rev. B 92 (2015) 054201.
[214] F. Zipoli et al., Phys. Rev. B 93 (2016) 115201.
[215] H. Li, J. Robertson, Appl. Phys. Lett. 116 (2020) 052103.
[216] D. Krebs et al., New J. Phys. 16 (2014) 043015.
[217] P. Noé et al., J. Phys. D Appl. Phys. 49 (2016) 035305.
[218] G.C. Sosso et al., J. Phys. Chem. B 118 (2014) 13621.
[219] G.P. Johari, M. Goldstein, J. Chem. Phys. 53 (1970) 2372.
[220] C.A. Angell, Science 267 (1995) 1924.
[221] M. Micoulaut, Rep. Prog. Phys. 79 (2016) 066504.
[222] W.H. Wang, Prog. Mater Sci. 106 (2019) 100561.
[223] S.-X. Peng et al., Sci. Adv. 6 (2020) eaay6726.
[224] B. Zhang et al., Appl. Phys. Lett. 108 (2016) 191902.
[225] M. Xu et al., PNAS 109 (2012) E1055.
[226] S. Caravati et al., J. Phys.: Condens. Matter 21 (2009) 255501.
[227] K. Konstantinou et al., Nat. Commun. 10 (2019) 3065.
[228] F.C. Mocanu et al., J. Phys. Chem. B 122 (2018) 8998.
[229] M. Krbal et al., Phys. Rev. B 83 (2011) 054203.
[230] M. Krbal et al., Appl. Phys. Lett. 102 (2013) 111904.
[231] K.V. Mitrofanov et al., J. Appl. Phys. 115 (2014) 173501.
[232] A. Lotnyk et al., Acta Mater. 105 (2016) 1.
[233] A. Hirata et al., Phys. Rev. Lett. 120 (2018) 205502.
[234] S. Ambrogio et al., Nature 558 (2018) 60.
[235] S. Kim et al., IEDM Technol. Dig. (2013) 30.7.1.
[236] W.W. Koelmans et al., Nat. Commun. 6 (2015) 8181.
[237] S. Kim et al., IEEE Trans. Elect. Dev. 63 (2016) 3922.
[238] D. Adler et al., J. Appl. Phys. 51 (1980) 3289.
[239] I. Giannopoulos et al., IEDM Technol. Dig. (2018) 27.7.1.
[240] J. Luckas et al., J. Appl. Phys. 113 (2013) 023704.
[241] C. Li et al., J. Mater. Chem. C 6 (2018) 3387.
[242] S. Caravati et al., J. Phys.: Condens. Matter 23 (2011) 265801.
[243] W. Kim et al., IEDM Technol. Dig. (2016) 4.2.1.
[244] S. Kim et al., MRS Bull. 44 (2019) 710.
[245] A. Padilla et al., J. Appl. Phys. 110 (2011) 054501.
[246] Y. Xie et al., Adv. Mater. 30 (2018) 1705587.
[247] M. Cobelli et al., J. Phys. Chem. C 124 (2020) 9599.
[248] K. Ding et al., Science 366 (2019) 210.
[249] Q.H. Wang et al., Nat. Nanotechnol. 7 (2012) 699.

[250] M. Chhowalla et al., Nat. Chem. 5 (2013) 263.
[251] S. Manzeli et al., Nat. Rev. Mater. 2 (2017) 17033.
[252] T.-T. Jiang et al., APL Mater. 7 (2019) 081121.
[253] C.E. Giusca et al., Nano Lett. 13 (2013) 4020.
[254] W.H. Wang et al., Surf. Coat. Technol. 177–178 (2004) 795.
[255] M. Mitra et al., Appl. Phys. Lett. 96 (2010) 222111.
[256] M. Salinga et al., Nat. Mater. 17 (2018) 681.
[257] F. Jiao et al., Appl. Mater. Today 20 (2020) 100641.
[258] W. Zhang, E. Ma, Nat. Mater. 17 (2018) 654.
[259] V.L. Deringer et al., Adv. Mater. 31 (2019) 1902765.
[260] J. Behler, Angew. Chem. Int. Ed. 56 (2017) 12828.
[261] G.C. Sosso et al., J. Phys. Chem. Lett. 4 (2013) 4241.
[262] G.C. Sosso et al., J. Phys. Chem. C 119 (2015) 6428.
[263] S. Gabardi et al., Faraday Discuss. 213 (2018) 287.
[264] G.C. Sosso et al., Phys. Status Solidi A 213 (2016) 329.
[265] G.C. Sosso et al., Phys. Rev. B 86 (2012) 104301.
[266] E. Bosoni et al., J. Phys. D Appl. Phys. 53 (2020) 054001.
[267] F. Zipoli, A. Curioni, New J. Phys. 15 (2013) 123006.
[268] G.C. Sosso et al., Phys. Rev. B 85 (2012) 174103.
[269] G.C. Sosso, M. Bernasconi, MRS Bull. 44 (2019) 705.
[270] F.C. Mocanu et al., J. Phys. D Appl. Phys. 53 (2020) 244002.
[271] S. Gabardi et al., J. Phys. Chem. C 121 (2017) 23827.
[272] L. Ward et al., Acta Mater. 159 (2018) 102.
[273] D.R. Cassar et al., Acta Mater. 159 (2018) 249.
[274] N.M. Anoop Krishnan et al., J. Non-Cryst. Solids 487 (2018) 37.
[275] S.V. Ketov et al., Nature 524 (2015) 200.

[276] J. Pan et al., Nature 578 (2020) 559.
[277] G. Ding et al., Sci. Adv. 5 (2019) eaaw6249.
[278] A. Kolobov et al., Phys. Rev. Lett. 97 (2006) 035701.
[279] S. Caravati et al., Phys. Rev. Lett. 102 (2009) 205502.
[280] Z. Sun et al., PNAS 108 (2011) 10410.
[281] K. Xu et al., Phys. Status Solidi RRL 13 (2019) 1800506.
[282] S.M.S. Privitera et al., Phys. Rev. B 94 (2016) 094103.
[283] M. Zhu et al., MRS Bull. 44 (2019) 715.
[284] D.M. Kroll, Phys. Rev. B 9 (1974) 1669.
[285] V.G. Karpov et al., Appl. Phys. Lett. 90 (2007) 123504.
[286] D. Ielmini, Y. Zhang, J. Appl. Phys. 102 (2007) 054517.
[287] P. Noé et al., Sci. Adv. 6 (2020) eaay2830.
[288] M. Wuttig et al., Nat. Photon. 11 (2017) 465.
[289] D. Wright et al., MRS Bull. 44 (2019) 721.
[290] C. Ríos et al., Nat. Photon. 9 (2015) 725.
[291] Y. Zhang et al., Nat. Commun. 10 (2019) 4279.
[292] H. Zhang et al., ACS Photon. 6 (2019) 2205.
[293] C. Ríos et al., Sci. Adv. 5 (2019) eaau5759.
[294] Z. Cheng et al., Adv. Mater. 30 (2018) 1802435.
[295] Z. Cheng et al., Sci. Adv. 3 (2017) e1700160.
[296] J. Feldmann et al., Nature 569 (2019) 208.
[297] P. Hosseini et al., Nature 511 (2014) 206.
[298] J. Tian et al., Nat. Commun. 10 (2019) 396.
[299] P. Li et al., Nat. Mater. 15 (2016) 870.
[300] B. Gholipour, Science 366 (2019) 186.